Efficient immersed-boundary lattice Boltzmann scheme for fluid-structure interaction problems involving large solid deformation

Yunan Cai, Shuangqiang Wang, Jianhua Lu,[*,†] Sheng Li,[†] and Guiyong Zhang[†]

State Key Laboratory of Structural Analysis for Industrial Equipment, School of Naval Architecture,
Faculty of Vehicle Engineering and Mechanics, Dalian University of Technology,
Dalian 116024, People's Republic of China

A hybrid numerical method which couples the immersed-boundary lattice Boltzmann method with the smoothed point interpolation method (S-PIM) is presented in this paper for the fluid-structure interaction problems involving large solid deformation. In the method, the lattice Boltzmann method is adopted for its advantages in modeling complex fluid flow, the S-PIM is coupled for its robustness in dealing with large solid deformation, and the immersed-boundary method is used for its efficiency in handling the interaction of fluid and solid. In the fluid-solid coupling procedure, a force correction technique based direct-forcing scheme is introduced to enforce nonslip boundary condition with high accuracy, and an averaged dual time stepping scheme is proposed to get stronger robustness of the present method. Numerical experiments are carefully carried out from benchmark problems such as cylinder Couette flow and a beam in a fluid tunnel to more challenging problems such as a flexible beam in the wake of a cylinder and the swimming of a two-dimensional fishlike body. Comparisons of the numerical results with the referenced solutions show that all desirable features of these coupled methods are inherited in the present coupling scheme, and the efficiency of the present method to model such complex problems is verified.

I. INTRODUCTION

Numerical modeling of fluid-structure interaction (FSI) problems is one of the key topics in the field of computational fluid dynamics due to its wide spread in nature and vast applications in many industrial fields. The requirement to couple fluid dynamics and solid mechanics poses a challenging task in developing related numerical methods. Among the existing methods, the immersed-boundary method (IBM) has been proven to be an efficient one since it was first proposed by Peskin [1] in the 1970s to simulate the heart blood flow. In this method, the governing equations of fluid field are solved on a fixed Eulerian grid and the moving solid boundary is discretized to a set of Lagrangian points. The interactions of the fluid and solid at the interfaces are modeled by introducing a body force term to the fluid domain adjacent to the immersed-boundary points. Unlike the conventional body fitted methods, the remeshing procedure, which is computationally costly, is avoided in the IBM [2]. Meanwhile, the additional errors no longer exist which are brought by the conventional body fitted methods when they transfer data from the old mesh to the new one [3]. In addition, the method is mainly focused on the fluid-solid interaction treatment, and one can have much flexibility in selecting the numerical methods for fluid flow and solid deformation modeling. Such advantages of the IBM

enable its efficiency in the FSI problems, especially when large boundary deformations are involved.

Many IBM versions in different numerical frameworks for fluid flow or solid modeling have been proposed in the last few decades [2–11]. One category of the IBM, namely the immersed-boundary lattice Boltzmann method (IB-LBM), has been proposed in the last decade, which was first introduced by Feng and Michaelides [6] for the fluid-particle interaction problem. In the IB-LB framework, a mesoscopic method based on kinetics theory, the lattice Boltzmann method, is utilized for fluid flow modeling considering many of its distinguished features, such as a clear physical picture of fluid flow, simplicity in complex boundary treatment, and natural parallelism [12]. The advantages of the IBM and LBM are inherited in the coupling scheme, which enables it to be a promising tool to handle complex FSI problems [13].

In general, different versions of the IB-LBM mainly differ from each other by the boundary force calculation methods they adopt to implement the fluid-solid interaction efficiently, which is also the main issue in the development of the IBM in the framework of the LBM. In Feng and Michaelides's work [6], Hook's law is used to calculated the boundary force by estimating the displacement of the solid boundaries. The solid velocity is interpolated from the velocities of fluid flow nearby. It should be noted that here the solid is assumed to have a fiber-like immersed elastic structure and the method is applicable only when the solid is quite soft and massless. To overcome the defect, Kim and Peskin [14] proposed the penalty method and Tian *et al.* [2] proposed a modified one which enables the IB-LBM to handle the fiber-like elastic structure with finite mass. However, an artificial spring parameter should be introduced to make such improvement. To

---

*Corresponding author: lujh@dlut.edu.cn

†Also at Collaborative Innovation Center for Advanced Ship and Deep-Sea Exploration, Shanghai 200240, People's Republic of China.

solve this problem, Yuan *et al.* [15] employed the momentum exchange method for boundary force calculation and applied it to the flexible filament simulations. In the method, the artificial parameter is eliminated and the boundary force can be calculated directly. The boundary velocity and displacement can be updated using Newton's second law. Although progress has been made, the above conventional IB-LBMs still cannot enforce the nonslip boundary conditions on the immersed boundaries due to the diffusive effect [16–19]. The numerical accuracy is heavily affected and the robustness problem usually appears when strong fluid-solid interactions need to be handled [16–18]. Many efforts have been devoted to the problem. For example, Luo *et al.* [20] and Wang *et al.* [21] proposed a multidirect forcing method in which several iterative steps are carried out in evaluating the force. Wu and Shu [16] presented an implicit velocity-correction scheme to enhance the nonslip boundary conditions by solving a linear equation system of boundary velocity residual. Hu *et al.* [18] improved the momentum exchange method based on an iterative IB-LBM framework and introduced a relaxation parameter to speed up the iteration procedure. Cheng *et al.* [22] proposed a semi-implicit immersed-boundary lattice Bhatnagar-Gross-Krook (IB-LBGK) coupling scheme by using the iterative technique in the coupling cycle to enhance the robustness of the method. However, all the improvements are achieved at the cost of large computational time increments.

As another important issue, the solid modeling in the IB-LBM was also addressed by many authors [2,3,7–10,14,15,22,23]. Up to now, most of existing works follow the original model in which the solid is described as a fiber-like elastic structure [2,14,15,22,23]. To expand it to more realistic solids and take the inner deformation of the solid into consideration, Kollmannsberger *et al.* [3] investigated the validity and efficiency of coupling the particle finite element method with the lattice Boltzmann method for transient bidirectional fluid-structure interaction problems. Kürger *et al.* [7] employed an IB-LB finite element method and analyzed its efficiency and accuracy for simulating multiple deformable particle problems. Rosis *et al.* [8,9] coupled the finite element method into the IB-LBM to handle the solid deformation involved in their simulations and applied it for aeroelastic study of flexible flapping wings. Dorschner *et al.* [10] proposed a fluid-structure interaction scheme combining a nonlinear finite element solver with the entropic multi-relaxation time lattice Boltzmann model. It should be noted that the robustness and accuracy of the finite element method (FEM) has strong dependence on the quality of the solid mesh, and when mesh distortion happens, the performance of the FEM may also be degraded [24]. In other words, developing a more efficient IB-LBM especially for fluid-solid interaction problems with large solid deformation is still open to the FSI numerical modeling community.

Recently, an improved IB-LBM [19] has been proposed for FSI problems. In the scheme, a force correction technique is introduced to enforce the nonslip boundary conditions at the immersed boundaries in a simple explicit way. Moreover, the viscosity dependence [25,26], which may lead to velocity error in the vicinity of the immersed boundaries, is reduced by employing a multiple relaxation times (MRT) based LBM model. The improved IB-LBM has superior performance in

terms of accuracy and computational efficiency. However, in the method, the solid domain is calculated based on the fiber-like assumption, which is incapable of dealing with realistic solid structure deformation. Moreover, the stiffness parameters of the boundary need to be chosen in a quite limited range or they would cause instability.

Meanwhile, a coupled IB-LBM and smoothed point interpolation method (S-PIM) have been introduced for FSI problems with large solid deformation [27]. In the method, the conventional direct-forcing IB-LBM framework is employed for the fluid flow and the fluid-solid interaction. As for the solid modeling, the S-PIM is adopted to solve the solid structure based on the realistic nonlinear constitutive law. As a mesh-free method, the S-PIM can resist large mesh distortion and it is suitable for the large solid deformation problems [28,29]. The coupled scheme is good at dealing with a realistic solid structure, but the nonslip boundary conditions at the immersed boundaries cannot be enforced accurately. What is more, the viscosity dependence is not considered, which may degrade the accuracy of the coupled scheme.

Thus a question appears: Is it possible to couple the two schemes which can integrate the most desired features of both but eliminate shortcomings of each? In this paper, such a coupled method is proposed. To this end, unlike the previous two schemes, the following improvements are made:

(1) The present work couples the force-correction-based IB-LBM with the S-PIM, in which the most desired features of the two methods are inherited.

(2) Compared with the original force-correction-based IB-LBM, the solid domain is modeled based on the nonlinear constitutive law; thus a realistic solid deformation can be considered. Moreover, by introducing a time-average technique to the solid boundary velocity calculation, a robustness improvement of the present coupling scheme is achieved.

(3) Compared with the original IB-LBM coupled with the S-PIM scheme, the nonslip boundary conditions at the immersed boundaries are enforced by the force correction technique and the viscosity dependence is dramatically reduced by an MRT-based LBM model.

To validate the present method, several numerical experiments are carried out, e.g., cylindrical Couette flow, a beam in a fluid tunnel, flow passing a cylinder with a flexible beam, together with discussions about the accuracy, computational efficiency, and robust properties of the proposed IB-LBM. In addition, the self-propelled fishlike body swimming problem is simulated as an application. The effects of muscle strength and the body stiffness on the fish's straight-line swimming speed are investigated numerically. The remaining sections of the paper are organized as follows: In Sec. II, the proposed coupled method is presented. In Sec. III, the numerical experiments and discussions are provided, and in Sec. IV, the conclusions are given.

II. COUPLED METHOD

In this section, the coupled force-correction-based IB-LBM with S-PIM scheme is introduced. In the coupled method, the fluid domain is solved by the LBM, and the fluid-solid interaction is handled by the IBM in the framework of the IB-LBM, which is introduced in Sec. II A. The solid
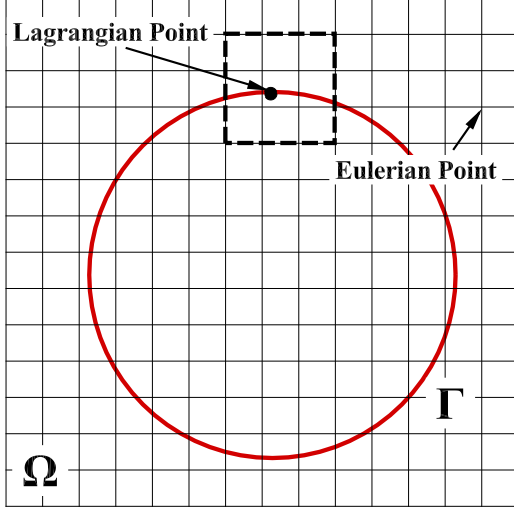
FIG. 1. Illustration of the immersed-boundary method. The boundary is represented by the Lagrangian points and fluid points are represented by the intersection points of mesh lines. The interaction area between the solid point and the fluid points is enclosed by dashed lines.

domain is modeled by the S-PIM based on the realistic nonlinear constitutive law, which is presented in Sec. II B. Section II C introduces the methods for the boundary force evaluation, which includes the force correction and the time-average coupling techniques. The dimensionless procedures are described specifically in Sec. II D. In Sec. II E, the summary of the algorithm implementation and main features of the coupling scheme are provided.

A. Immersed-boundary lattice Boltzmann method

In this section, the IB-LBM used in this work is briefly introduced. Before this, the basic idea of the IBM, which will be numerically solved in the framework of the lattice Boltzmann method, is illustrated by a two-dimensional fluid-structure interaction problem as an example. As shown in Fig. 1, a two-dimensional domain Ω is filled with viscous fluid, and the solid with boundary curve Γ is in it. In the IBM,

the fixed Eulerian grid is employed to calculate the fluid flow and the solid is represented by a series of Lagrangian points. The governing equations for the fluid flow can be written as

$$\nabla \cdot \mathbf{v}^f = 0, \tag{1}$$

$$\rho^f \left(\frac{\partial \mathbf{v}^f}{\partial t} + \mathbf{v}^f \cdot \nabla \mathbf{v}^f \right) = -\nabla p^f + \mu^f \nabla^2 \mathbf{v}^f + \mathbf{g}, \tag{2}$$

where $\mathbf{v}^f$ is the fluid velocity, ρ^f is the fluid density, p^f is the fluid pressure, and μ^f is the fluid dynamic viscosity. The basic idea of the IBM is to apply a body force term in the fluid at the neighboring domain of the solid boundary points to accommodate the fluid-solid interaction, which results in an extra body force term $\mathbf{g}$ in Eq. (2). The Dirac δ function is employed to interpolate the fluid velocity from the Eulerian points to the Lagrangian ones and distribute the boundary force from the Lagrangian ones to the Eulerian ones, which can be expressed as

$$\mathbf{v}^f(\mathbf{X}, t) = \int_\Omega \mathbf{v}^f(\mathbf{x}, t)\delta(\mathbf{x} - \mathbf{X})d\mathbf{x}, \tag{3}$$

$$\mathbf{g}(\mathbf{x}, t) = \int_\Gamma \mathbf{F}^{\mathrm{FSI}}(\mathbf{X}, t)\delta(\mathbf{x} - \mathbf{X})ds, \tag{4}$$

where $\mathbf{x}$ and $\mathbf{X}$ represent the Eulerian and Lagrangian coordinates, respectively. $\mathbf{F}^{\mathrm{FSI}}$ is the interaction surface force acting on the immersed boundaries.

To solve the governing equations above, the split-forcing lattice Boltzmann equation (LBE) proposed by Guo *et al.* [30] is adopted. The LBE is able to recover the Navior-Stokes equations with a second-order accuracy, which is consistent with the original LB model's accuracy [17,30]. The evolution equations are as follows:

$$
\begin{aligned}
&f_\alpha(\mathbf{x} + \mathbf{c}_\alpha \delta t, t + \delta t) - f_\alpha(\mathbf{x}, t) \\
&= -\frac{1}{\tau}\left[f_\alpha(\mathbf{x}, t) - f_\alpha^{eq}(\mathbf{x}, t)\right] + \left(1 - \frac{1}{2\tau}\right)F_\alpha \delta t, \quad (5)
\end{aligned}
$$

with

$$F_\alpha = \omega_\alpha \left(\frac{\mathbf{c}_\alpha - \mathbf{v}^f}{c_s^2} + \frac{\mathbf{c}_\alpha \cdot \mathbf{v}^f}{c_s^4}\mathbf{c}_\alpha \right) \cdot \mathbf{g}, \tag{6}$$

$$\mathbf{c}_\alpha = \begin{cases} (0,0), & \alpha = 0, \\ (\cos[(\alpha-1)\pi/2], \sin[(\alpha-1)\pi/2])c, & \alpha = 1,2,3,4, \\ \sqrt{2}(\cos[(2\alpha-9)\pi/4], \sin[(2\alpha-9)\pi/4])c, & \alpha = 5,6,7,8, \end{cases} \tag{7}$$

where f_α is the distribution function in the α direction, τ is the relaxation time, and $\mathbf{c}_\alpha$ are the discrete velocities for the D2Q9 model [31]. The grid velocity is $c = \delta x/\delta t$; sound velocity $c_s = c/\sqrt{3}$. f_α^{eq} is the equilibrium distribution function; here the He-Luo model [32] is employed, which can be written as

$$f_\alpha^{eq} = \omega_\alpha \left[\rho^f + \rho_0^f \left(\frac{\mathbf{c}_\alpha \cdot \mathbf{v}^f}{c_s^2} + \frac{(\mathbf{c}_\alpha \cdot \mathbf{v}^f)^2}{2c_s^4} - \frac{(\mathbf{v}^f)^2}{2c_s^2} \right) \right], \tag{8}$$

with $\omega_0 = 4/9$, $\omega_{1-4} = 1/9$, $\omega_{5-8} = 1/36$. ρ_0^f is the static density of the fluid. The density, velocity, and pressure can be evaluated as

$$\rho^f = \sum_{\alpha=0}^{8} f_\alpha, \tag{9}$$

$$\rho_0^f \mathbf{v}^f = \sum_{\alpha=0}^{8} \mathbf{c}_\alpha f_\alpha + \frac{1}{2}\mathbf{g}\delta t, \tag{10}$$

$$p^f = \rho^f c_s^2. \tag{11}$$

The kinematic viscosity ν is determined by

$$\nu = c_s^2\left(\tau - \tfrac{1}{2}\right)\delta t. \qquad (12)$$

For better numerical accuracy and stability, the lattice Boltzmann evolution equation based on MRT model [26], instead of the single relaxation time (SRT) model, is adopted as

$$f_\alpha(\mathbf{x} + \mathbf{c}_\alpha \delta t, t + \delta t) - f_\alpha(\mathbf{x}, t)$$
$$= -\mathbf{M}^{-1}\mathbf{S}(\mathbf{m} - \mathbf{m}^{eq}) + \mathbf{M}^{-1}(\mathbf{I} - \mathbf{S}/2)\mathbf{M}F_\alpha \delta t. \qquad (13)$$

As shown above, the collision step is executed in the momentum space $\mathbf{m} = m_k$, $k = 0, 1, \ldots, 8$, in the MRT-LBE instead of executing the collision step in velocity space $\mathbf{f} = f_k$, $k = 0, 1, \ldots, 8$, in the SRT. The relationship between $\mathbf{f}$ and $\mathbf{m}$ can be expressed as

$$\mathbf{m} = \mathbf{Mf}, \quad \mathbf{m}^{eq} = \mathbf{Mf}^{eq}. \qquad (14)$$

For the D2Q9 model, the transformation matrix $\mathbf{M}$ can be given as

$$\mathbf{M} = \begin{pmatrix} 1 & 1 & 1 & 1 & 1 & 1 & 1 & 1 & 1 \\ -4 & -1 & -1 & -1 & -1 & 2 & 2 & 2 & 2 \\ 4 & -2 & -2 & -2 & -2 & 1 & 1 & 1 & 1 \\ 0 & 1 & 0 & -1 & 0 & 1 & -1 & -1 & 1 \\ 0 & -2 & 0 & 2 & 0 & 1 & -1 & -1 & 1 \\ 0 & 0 & 1 & 0 & -1 & 1 & 1 & -1 & -1 \\ 0 & 0 & -2 & 0 & 2 & 1 & 1 & -1 & -1 \\ 0 & 1 & -1 & 1 & -1 & 0 & 0 & 0 & 0 \\ 0 & 0 & 0 & 0 & 0 & 1 & -1 & 1 & -1 \end{pmatrix}. \qquad (15)$$

$\mathbf{S} = \mathrm{diag}(0, s_e, s_\varepsilon, 0, s_q, 0, s_q, s_\nu, s_\nu)$ is the relaxation matrix. The parameter s_ν and the relaxation time τ have the following relationship:

$$s_\nu = \frac{1}{\tau}. \qquad (16)$$

To achieve expected numerical accuracy, it is crucial to choose the proper values of the relaxation parameters. Ginzburg and Adler [33] first proposed to choose the MRT model by using a certain formula between two relaxation time parameters; the exact solution can be obtained for a straight channel for the bounce-back boundary implementation method based LBM. In the IB-LBM framework, Le and Zhang [25] also found that the near boundary velocity becomes abnormal if the single relaxation time (SRT) based LB model is used, which will lead to serious numerical boundary slip. This unphysical phenomenon depends on the relaxation time parameter τ which corresponds to the fluid viscosity. This is the so called viscosity dependence. Lu *et al.* [26] proposed a multiple relaxation times (MRT) model to reduce the numerical slip by establishing a certain relationship between s_q and s_ν, which can be expressed as

$$s_q = \frac{4(2 - s_\nu)}{4 + 7s_\nu}. \qquad (17)$$

For s_e and s_ε, they can be set as

$$s_e = s_\varepsilon = s_\nu. \qquad (18)$$

In this paper, Lu *et al.*'s MRT model [26] is employed and its efficiency will be illustrated by a comparison with the SRT model in the numerical test of cylindrical Couette flow.

B. Smoothed point interpolation method

The well-known finite element method (FEM) has been widely used for a variety of solid dynamics problems, while the FEM model is inaccurate in stress solutions, especially with linear triangular or tetrahedral meshes. When the element mesh is heavily distorted, the standard FEM encounters a significant accuracy loss due to the strong dependency on mesh quality [24]. To solve such problems, the S-PIM models have been developed by using gradient smoothing technology with simple triangular or tetrahedral meshes. In these models, the accuracy of the displacement and the stress solution can be improved significantly. In addition, the intensity to mesh distortion has been enhanced for large deformation due to softened model stiffness in the S-PIM [29]. As one of such models, the edge-based smoothed point interpolation method (ES-PIM) has shown its superiority in the S-PIM family [28]. The theoretical rate of convergence of the solution error in the L^2 norm of the ES-PIM is expected to be 2.0 [29]. Thus the ES-PIM is employed in the present IB-LBM to utilize its efficiency for modeling large deformation involved solids.

1. Solid governing equations

The ES-PIM adopted here is mainly used to deal with the deformation of nonlinear solids. The governing equation for the nonlinear solid can be expressed as

$$\rho^s \frac{\partial^2 \mathbf{u}^s}{\partial t^2} = \frac{\partial \mathbf{P}^s}{\partial \mathbf{X}^s} + \rho^s \mathbf{g}, \qquad (19)$$

where ρ^s is the solid density, $\mathbf{u}^s$ denotes the displacement of the solid, and $\mathbf{P}^s$ refers to the first Piola-Kirchhoff stress. The solid displacement $\mathbf{u}^s$, velocity $\mathbf{v}^s$, and acceleration $\mathbf{a}^s$ can be interpolated using the point interpolation function Φ_I^s as [34,35]

$$\mathbf{u}^s = \sum_I \Phi_I^s \mathbf{u}_I^s, \quad \mathbf{v}^s = \sum_I \Phi_I^s \mathbf{v}_I^s, \quad \mathbf{a}^s = \sum_I \Phi_I^s \mathbf{a}_I^s. \qquad (20)$$

Substituting Eq. (20) into Eq. (19) and implementing the Galerkin procedure, the motion equation of the solid can be written as follows:

$$\mathbf{M}_{IJ}^s \mathbf{a}_J^s = \mathbf{f}_I^{\mathrm{ext}} - \mathbf{f}_I^{\mathrm{int}}, \qquad (21)$$

with

$$\mathbf{f}_I^{\mathrm{int}} = \int_{0\Omega_s} {}^0\mathbf{B}_I^T \mathbf{S} d\Omega, \quad \mathbf{f}_I^{\mathrm{ext}} = \int_{0\Omega_s} \Phi_J^s \rho^s \mathbf{b} + \int_{0\Gamma_s} \Phi_J^s \bar{\mathbf{T}} d\Gamma, \qquad (22)$$

where $\mathbf{M}_{IJ}^s$ is the lumped mass matrix, $\mathbf{a}_J^s$ is the solid acceleration vector, and $\mathbf{f}_I^{\mathrm{int}}$ and $\mathbf{f}_I^{\mathrm{ext}}$ are the internal and external force vectors, respectively. $\mathbf{b}$ is the body force, for example, gravity force. $\bar{\mathbf{T}}$ is the boundary force, such as the FSI force.

$\mathbf{S}$ is the second Piola-Kirchhoff stress, and ${}^0\mathbf{B}_I^T$ is the strain-displacement matrix which includes two components [36]:

$$
{}^0\mathbf{B}_{I0}^{J_i} = \begin{bmatrix} \dfrac{\partial \Phi_{J_i}^s}{\partial X^s} & 0 \\[2ex] 0 & \dfrac{\partial \Phi_{J_i}^s}{\partial Y^s} \\[2ex] \dfrac{\partial \Phi_{J_i}^s}{\partial Y^s} & \dfrac{\partial \Phi_{J_i}^s}{\partial X^s} \end{bmatrix}, \tag{23}
$$

$$
{}^0\mathbf{B}_{I1}^{J_i} = \begin{bmatrix} \dfrac{\partial \Phi_I^s}{\partial X^s}\dfrac{\partial x_{J_i}^s}{\partial X^s} & \dfrac{\partial \Phi_I^s}{\partial X^s}\dfrac{\partial y_{J_i}^s}{\partial X^s} \\[2ex] \dfrac{\partial \Phi_I^s}{\partial Y^s}\dfrac{\partial x_{J_i}^s}{\partial Y^s} & \dfrac{\partial \Phi_I^s}{\partial Y^s}\dfrac{\partial y_{J_i}^s}{\partial Y^s} \\[2ex] \dfrac{\partial \Phi_I^s}{\partial X^s}\dfrac{\partial x_{J_i}^s}{\partial Y^s} + \dfrac{\partial \Phi_I^s}{\partial Y^s}\dfrac{\partial x_{J_i}^s}{\partial X^s} & \dfrac{\partial \Phi_I^s}{\partial X^s}\dfrac{\partial Y_{J_i}^s}{\partial Y^s} + \dfrac{\partial \Phi_I^s}{\partial Y^s}\dfrac{\partial Y_{J_i}^s}{\partial X^s} \end{bmatrix}, \tag{24}
$$

where ${}^0\mathbf{B}_{I0}^{J_i}$ represents the initial state and ${}^0\mathbf{B}_{I1}^{J_i}$ represents the increment during deformation.

2. Nonlinear constitutive model

The isotropic Saint Venant–Kirchhoff model is used to calculate the Piola-Kirchhoff (PK2) stress. The strain energy density function can be expressed as

$$
w = \tfrac{1}{2}\lambda(\operatorname{tr}\mathbf{E})^2 + \mu \operatorname{tr}(\mathbf{E})^2, \tag{25}
$$

where λ and ν are Lam constants, and $\mathbf{E}$ is the Green strain tensor. The PK2 stress can be calculated by

$$
\mathbf{S} = \frac{\partial w}{\partial \mathbf{E}}, \quad \mathbf{E} = \frac{1}{2}(\mathbf{F}^T\mathbf{F} - \mathbf{I}), \tag{26}
$$

where $\mathbf{I}$ is the unit matrix and $\mathbf{F}$ is the deformation gradient which has the following relationship with the displacement gradient $\mathbf{u}_{i,j}$:

$$
\mathbf{F} = \mathbf{u}_{i,j} + \mathbf{I}. \tag{27}
$$

3. The gradient smoothing technique in S-PIM

The gradient smoothing operation is introduced in the S-PIM to soften the model stiffness, which has been overestimated in the FEM with a T3 element [29]. Supposed the solid domain ${}^0\Omega^s$ is divided into N_{sd}^s non-overlapping smoothing domains ${}^0\Omega_{isd}^{sd}$ with boundaries ${}^0\Gamma_{isd}^{sd}$. As shown in Fig. 2, based on the discrete T3 elements, edge-based smoothing domains can be constructed by combining edge points with the centroid points of the adjacent elements. The smoothed displacement gradient in ${}^0\Omega_{isd}^{sd}$ can be evaluated as

$$
\bar{u}_{i,j}^s(\mathbf{x}_l) = \int_{{}^0\Omega_{isd}^{sd}} u_{i,j}^s(\xi)W(\mathbf{x}_l - \xi)d\Omega, \tag{28}
$$

with

$$
W(\mathbf{x}_l - \xi) = \begin{cases} 1/A_{isd}^{sd}, & \xi \in {}^0\Omega_{isd}^{sd}, \\ 0, & \xi \notin {}^0\Omega_{isd}^{sd}, \end{cases} \tag{29}
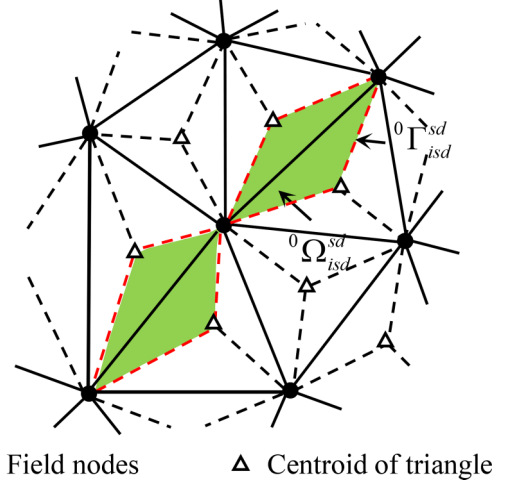$$

● Field nodes   △ Centroid of triangle

FIG. 2. Edge-based smoothing domain construction.

where $\bar{u}_{i,j}^s(\mathbf{x}_l)$ is the smoothed displacement gradient. $\mathbf{x}_l$ are the coordinates of the element node. ξ represents the position of any point in the smoothing domain. $W(\mathbf{x}_l - \xi)$ is the smoothing function and A_{isd}^{sd} is the smoothing area. By employing the divergence theorem, Eq. (28) can be rewritten as

$$
\bar{u}_{i,j}^s(\mathbf{x}_l) = \sum_I \left(\frac{1}{A_{isd}^{sd}} \int_{{}^0\Gamma_{isd}^{sd}} \Phi_I^s(x^s)n_j^{sd}d\Gamma \right)u_{Ii}^s, \tag{30}
$$

where n_j^{sd} is the outward surface normal of the smoothing domain boundary ${}^0\Gamma_{isd}^{sd}$, and I is the number of nodes in the smoothing domain.

It has been found in Eq. (30) that the derivation of shape function has been avoided using the gradient smoothing technique. Therefore, compatible variable gradients have been replaced by smoothed gradients in the S-PIM, such as the smoothed displacement gradient in Eq. (30). And the smoothed deformation gradient can be calculated easily using smoothed displacement gradient in Eq. (27). Other smoothed variables, like the smoothed Green strain and the smoothed PK2 stress, can also be obtained in Eq. (26). It has been verified that the S-PIM can achieve a softened and more close-to-exact stiffness model compared to the FEM through a mass of numerical tests, which guarantees the numerical results with good convergence, accuracy, and efficiency [28].

C. Boundary force evaluation

1. Force correction technique

To evaluate the FSI force $\mathbf{F}^{\mathrm{FSI}}$ in a simple and accurate approach, a force correction technique [19] is adopted in the present paper. The method is in the framework of the direct-forcing method. The FSI surface force can be obtained as

$$
\mathbf{F}^{\mathrm{FSI}}(\mathbf{X}, t) = \frac{2\rho^f h_f}{\delta t}k(\mathbf{X}, t)[\mathbf{v}^s(\mathbf{X}, t) - \mathbf{v}_{\mathrm{nof}}(\mathbf{X}, t)], \quad \mathbf{X} \in \Gamma, \tag{31}
$$

with

$$k(\mathbf{X}, t) = \frac{1}{\sum_{i,j} \sum_{b=1}^{N} \delta(\mathbf{x}_{ij} - \mathbf{X}_b)\delta(\mathbf{x}_{ij} - \mathbf{X})\Delta s h_f^3}, \quad (32)$$

where $\mathbf{X}$ and $\mathbf{x}$ denote the coordinates of the Lagrangian point and the Eulerian point, respectively. $k(\mathbf{X}, t)$ is the force correction coefficient and h_f is the fluid grid size. Δs is the arc length between two adjacent IB points. N is the total number of the Lagrangian points. $\mathbf{v}^s$ is the solid velocity and $\mathbf{v}_{\mathrm{nof}}$ is the fluid velocity without the boundary force, which can be evaluated as

$$\rho_0^f \mathbf{v}_{\mathrm{nof}}(\mathbf{x}, t) = \sum_{\alpha=0}^{8} \mathbf{c}_\alpha f_\alpha(\mathbf{x}, t), \quad (33)$$

$$\mathbf{v}^f(\mathbf{X}, t) = \sum_{ij} \mathbf{v}^f(\mathbf{x}_{ij}, t)\delta(\mathbf{x}_{ij} - \mathbf{X})h_f^2. \quad (34)$$

The detailed derivation of the force correction coefficient can be found in Ref. [19]. After evaluating the FSI force, $\mathbf{F}^{\mathrm{FSI}}$ is distributed to the Eulerian points as

$$\mathbf{g}(\mathbf{x}, t) = \sum_{b=1}^{N} \mathbf{F}^{\mathrm{FSI}}(\mathbf{X}_b, t)\delta(\mathbf{x} - \mathbf{X}_b)\Delta s. \quad (35)$$

Finally, the fluid velocities at the Eulerian points are corrected as

$$\mathbf{v}^f(\mathbf{x}, t) = \mathbf{v}_{\mathrm{nof}}(\mathbf{x}, t) + \frac{\mathbf{g}(\mathbf{x}, t)\delta t}{2\rho^f}. \quad (36)$$

In actual implementation, the Dirac delta function is smoothly approximated by a continuous kernel distribution δ_h proposed by Peskin [37]:

$$\delta_h(\mathbf{x} - \mathbf{X}) = \frac{1}{h_f^2}\Phi\left(\frac{x_i - X_i}{h_f}\right)\Phi\left(\frac{y_j - Y_j}{h_f}\right), \quad (37)$$

with

$$\Phi(r) = \begin{cases} \frac{1}{8}\left(3 - 2|r| + \sqrt{1 + 4|r| - 4r^2}\right), & 0 \leqslant |r| < 1, \\ \frac{1}{8}\left(5 - 2|r| - \sqrt{-7 + 12|r| - 4r^2}\right), & 1 \leqslant |r| < 2, \\ 0, & |r| \geqslant 2, \end{cases} \quad (38)$$

where (x_i, y_j) and (X_i, Y_j) are the coordinates of the Eulerian point $\mathbf{x}$ and the Lagrangian point $\mathbf{X}$, respectively.

By employing the force correction technique, the FSI force is evaluated more accurately so the nonslip boundary condition is much better enhanced compared to the conventional IB-LBMs. In addition, the force correction coefficients are calculated in an explicit way; the computational cost is reduced compared with the implicit way [16], especially for complex problems with large scales of Lagrangian points. When the force correction coefficients are set to be 1 for all the IB points, the present force correction technique based scheme reduces to the conventional direct-forcing scheme [17].

2. Time-average coupling technique

In actual implementation for FSI problems with large deformable boundaries, generally, the time step of solid solver δt_s is smaller than that of the fluid solver δt_f to ensure stability. To synchronize the fluid and solid solvers, one can set $\delta t_f = \delta t_s$. But this choice would lead to large computational cost for the fluid solving procedure and it is obviously not practical. An alternative is to employ a dual time stepping approach, in which the fluid and the solid solvers have different simulation time steps. In this case, a number of subcycles are performed for the solid solver within one fluid step. The number of subcycles in one LBM step is determined by the fluid-solid time step ratio: $n_0 = \delta t_f / \delta t_s$. Using the subcycling procedure, the solid solver can be given as follows (i from 0 to $n_0 - 1$, and $\mathbf{v}_{t+\delta t_f}^{\mathrm{nof}}$ has been obtained after the LBM evolution):

$$\text{Surface force evaluation}: \bar{\mathbf{T}}_{t+\frac{i}{n_0}\delta t_f} = \frac{2\rho^f h_f k_t}{\delta t_f}\left(\mathbf{v}_{t+\frac{i}{n_0}\delta t_f}^s - \mathbf{v}_{t+\delta t_f}^{\mathrm{nof}}\right), \quad (39)$$

$$\text{S-PIM}: \left(\mathbf{X}_{t+\frac{i+1}{n_0}\delta t_f}^s, \mathbf{v}_{t+\frac{i+1}{n_0}\delta t_f}^s\right) = \Psi\left(\mathbf{X}_{t+\frac{i}{n_0}\delta t_f}^s, \mathbf{v}_{t+\frac{i}{n_0}\delta t_f}^s, \bar{\mathbf{T}}_{t+\frac{i}{n_0}\delta t_f}\right), \quad (40)$$

where $\mathbf{X}^s$ and $\mathbf{v}^s$ represent the solid position and velocity, respectively. The FSI force is evaluated as

$$\mathbf{F}_{t+\delta t_f}^{\mathrm{FSI}} = \frac{2\rho^f h_f k_{t+\delta t}}{\delta t_f}\left(\mathbf{v}_{t+\delta t_f}^s - \mathbf{v}_{t+\delta t_f}^{\mathrm{nof}}\right). \quad (41)$$

After that, $\mathbf{F}^{\mathrm{FSI}}$ is used to obtain the boundary body force term exerting on the Eulerian points with Eq. (4) and then the fluid velocity is corrected with Eq. (10). The subcycling procedure based coupling scheme brings greater flexibility in the choice of simulation time steps for the LBM and S-PIM, and provides an efficient way to synchronize the fluid and solid solvers. However, the coupling procedures are found to have poor numerical stability when the problems simulated involve the deformable boundaries, in which the motions of the boundaries are unprescribed. In our previous work [19],

the 4-step Runge-Kutta method is adopted to solve the above coupling equations. It should be noted that the solid and the fluid domains have to be solved for several times in one Runge-Kutta difference procedure. It would be quite complicated to implement for the present IB-LBM as the S-PIM has a much higher algorithm complexity than the fiber-like assumption based solid solver used in Ref. [19].

To get better numerical stability in a relatively simple way, a time-averaging coupling procedure is proposed in the present work to improve the robustness of the coupling algorithm. Assume that when the fluid simulation time approaches from t to $t + \delta t_f$, the solid domain undergoes an n_0 subcycling calculation. In the time-averaging coupling procedure, the solid boundary velocity $\mathbf{v}_{t+\frac{i}{n_0}\delta t_f}^s$ at each subcycling calculation is recorded first, where i represents the ith subcycling for the

solid solver. Then the FSI surface force for fluid is obtained with the time-average solid velocity $\bar{\mathbf{v}}^s$ as

$$\mathbf{F}^{\text{FSI}}_{t+\delta t_f} = \frac{2\rho^f h_f k_{t+\delta t}}{\delta t_f}\left(\bar{\mathbf{v}}^s_{t+\delta t_f} - \mathbf{v}^{\text{nof}}_{t+\delta t_f}\right), \tag{42}$$

with

$$\bar{\mathbf{v}}^s_{t+\delta t_f} = \frac{\sum_{i=0}^{n_0}\mathbf{v}^s_{t+\frac{i}{n_0}\delta t_f}}{n_0+1}. \tag{43}$$

In other words, we use the mean value of $\mathbf{v}^s$ from t to $t+\delta t_f$ to substitute for $\mathbf{v}^s(\mathbf{X}, t+\delta t_f)$ and then the FSI force term at $t+\delta t_f$ can be obtained using Eq. (42) rather than Eq. (41), which is the basic idea of the time-average coupling scheme. The instability of the coupling scheme may due to the artificial energy created at the fluid-solid interface [3]. In actual implementation, it is found that the artificial energy is dramatically reduced when employing the time-average technique and the stability is improved. More specific verifications are carried out in Secs. III B and III C.

D. Dimensionless procedures

In the present work, the equations in Sec. II A are considered dimensionless, which means no physical dimension is assigned to the variables and they are treated as pure numbers. Meanwhile the solid solver in Sec. II B uses the real physical parameters. When the coupling procedure is implemented, the variables employed from the solid solver to the fluid solver should be non-dimensionalized. Inversely, the dimensionalizing procedure is conducted when the solid solver employs the variables from the fluid solver.

The non-dimensionalizing and dimensionalizing procedures are carried out according to the scaling factors, which are defined as

$$C_l = \frac{l_{ph}}{l_{LB}}, \quad C_t = \frac{t_{ph}}{t_{LB}}, \quad C_\rho = \frac{\rho_{ph}}{\rho_{LB}}, \tag{44}$$

where C_l, C_t, and C_ρ are the basic scaling factors for length, time, and density. The subscripts refer to the physical or LB variables. For example, defining h_{LB} and δt_{LB} as the grid size and time step for LBM system, the corresponding length and time in the real physical system can be written as

$$h_{ph} = h_{LB}C_l, \quad \delta t_{ph} = \delta t_{LB}C_t. \tag{45}$$

It should be noted that other scaling factors, such as C_u and C_ν, are determined by the basic ones, which can be written as

$$C_u = \frac{C_l}{C_t} = \frac{v_{ph}}{v_{LB}}, \quad C_\nu = \frac{C_l^2}{C_t} = \frac{\nu_{ph}}{\nu_{LB}}, \tag{46}$$

where v and ν are the fluid velocity and kinematic viscosity, respectively.

These scaling factors are defined according the specific problems simulated and they are are chosen to be able to ensure stability in the simulations. All the scaling factors for each numerical test are provided in Sec. III.

E. Summary of the coupled method

The coupling illustration of the IB-LBM with the S-PIM is presented in Fig. 3, which provides the specific procedures
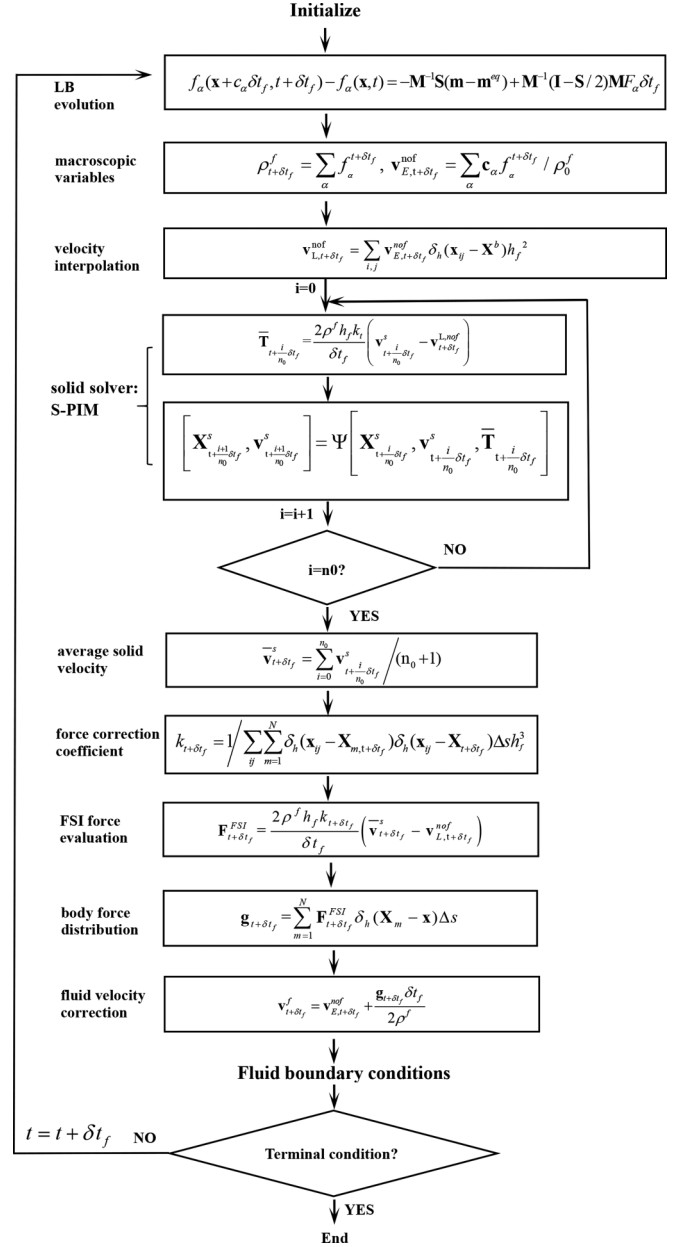

FIG. 3. Algorithm diagram of the present coupling scheme.

for the implementation of the present method. The coupling scheme enables the present method to simulate FSI problems involving large deformable solids in an efficient way. Some remarks of the features of the present method are given as follows.

Remark 1: Accuracy. In the FSI force evaluation procedure of the present coupling algorithm, a force correction coefficient is introduced, which improves the accuracy of the nonslip boundary condition enforcement at the IB points compared with the conventional direct-forcing scheme. Moreover, the MRT-based LB evolution equation proposed by Lu *et al.* [26] is employed rather than the SRT-model-based one which enables the present method to reduce the numerical boundary slip.

Remark 2: Robustness. The S-PIM is employed to solve the solid domain based on the nonlinear constitutive law, which

enables the present method to model a realistic solid rather than the fiber-like structure. In addition, the time-average technique is proposed in the present coupling scheme when evaluating the FSI force and this procedure can significantly improve the robustness of the algorithm.

Remark 3: Computational efficiency. The coupling procedure of the present algorithm is explicit; thus much computational cost can be saved compared with the implicit IB-LBMs with the same mesh size, while comparable accuracy with the implicit IB-LBMs can be obtained.

The above properties of the present method will be verified in the numerical experiments detailed in the following section.

III. NUMERICAL EXPERIMENTS

In this section, four numerical tests are carried out. The first one is the cylindrical Couette flow, which is a problem with analytical solutions. The spatial convergence properties of the present method are tested and the numerical accuracy improvement of the velocity profiles near the immersed boundary owing to the adopted MRT model is discussed as well. The second one is a rigid or elastic beam in the fluid, which is a static state problem. The accuracy of enforcing the nonslip boundary condition, the computational efficiency, and the robustness of the present method are demonstrated. The third numerical experiment is a flexible beam flapping in the wake of the cylinder, which is a more challenging unsteady FSI problem. The accuracy and stability of the present scheme for such transient cases are investigated through a spatial convergence study and the observation of the artificial energy created at the fluid-solid interface. Finally, the capability of the present method is proved for much more complex FSI problems by simulating a self-propelled fishlike body.

A. Cylindrical Couette flow

To test the spatial convergence properties and the immunity to the viscosity dependence of the proposed method, the cylindrical Couette flow is simulated. The sketch of the problem is illustrated in Fig. 4. As Fig. 4 shows, a solid ring is immersed in a squared fluid domain and it rotates with a constant velocity of $\omega^s = 2$ rad/s. The fluid inside and outside the ring undergoes a rotating motion around the center of the ring. If the flow remains laminar, the analytical angular velocity of the fluid particles inside the ring should be $\omega^f = 2$ rad/s. The exterior and interior radius of the ring are $R1 = 0.5$ cm and $R2 = 0.4$ cm. The size of the fluid domain is chosen as $8R1 \times 8R1$. The center of the ring is at $(4R1, 4R1)$. The values of the parameters for solid properties are set as follows: density $\rho_s = 10$ g/cm³, Young's modulus $E^s = 1 \times 10^4$ g/(cms²), and Poisson ratio $\nu^s = 0.3$. Gravity is neglected in this problem. The fluid density is chosen as $\rho_f = 1$ g/cm³. Two cases with different kinetic viscosities—case 1, $\nu^f = 0.1$ cm²/s and case 2, $\nu^f = 10$ cm²/s—are considered. The deformation of the ring is small enough with the large Young's modulus that the ring can be seen as rigid and the analytical resolutions can be employed to verify the accuracy of the numerical results.

The general periodic boundary conditions are used for all the outer boundaries. The problem is simulated by both
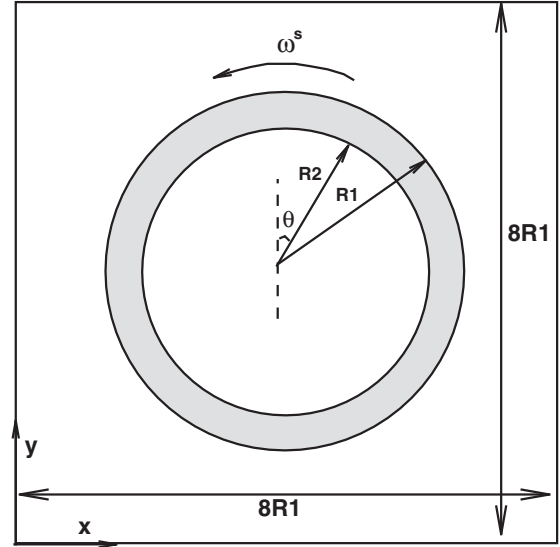

FIG. 4. Sketch of the cylindrical Couette flow.

the MRT- and SRT-based IB-LBMs for the purpose of the numerical comparison. As for the MRT model, the relaxation time parameters are chosen following Lu *et al.*'s work [26].

In this simulation, the non-dimensionalizing and dimensionalizing procedures are carried out according to Eq. (44) and Eq. (46). The basic scaling factors are set as $C_l = 1$ cm, $C_t = 0.01$ s, $C_\rho = 1$ g/cm³. Other scaling factors can be obtained as $C_u = \frac{C_l}{C_t} = 100$ cm/s, $C_\nu = C_u C_l = 100$ cm²/s.

Four different mesh sizes are employed: MS1, $h_f = 1/20$ cm, $h_s = 1/30$ cm; MS2, $h_f = 1/25$ cm, $h_s = 1/37.5$ cm; MS3, $h_f = 1/40$ cm, $h_s = 1/60$ cm; MS4, $h_f = 1/50$ cm, $h_s = 1/75$ cm; MS5, $h_f = 1/80$ cm, $h_s = 1/120$ cm, where h_f and h_s are the mesh spaces of fluid and solid, respectively. The $L2$ norm of the error for the fluid velocity is defined as $e_v = ||\mathbf{v}^a - \mathbf{v}^{num}||_{L2}/||\mathbf{v}^a||_{L2}$, where $\mathbf{v}^{num}$ and $\mathbf{v}^a$ are the numerical and analytical fluid velocities. The real physical simulation time is set to be $T = 10$ s and the convergent steady state of the fluid velocity is achieved at $t = T$.

First, the fluid velocity errors along the line $\theta = 0$ are observed. Figure 5(a) shows the spatial convergence properties of the present method with the MRT and SRT models in terms of the fluid velocity errors along the line $\theta = 0$. The slope of the convergence curve reveals the relationship of the error and the mesh size. It can be observed that in the case $\nu^f = 0.1$ cm²/s, the slopes of the convergence curves of the MRT and SRT models are about 2. This means the spatial truncation error for the coupled method is $R = o(h^2)$ and the method is of second-order accuracy. However, in the case $\nu^f = 10$ cm²/s, the accuracy of the SRT model deteriorates, while the MRT model still has good performance. What is more, for the two different cases, the MRT model has smaller errors than the SRT model. When the mesh gets finer, the MRT model can reach second-order accuracy and the errors are shown to be nearly independent of the fluid kinetic viscosity.

We further investigate the fluid tangential velocity profiles along the line $\theta = 0$ in Fig. 5(b). It is illustrated that the fluid velocity near the boundary shows apparent derivation to the
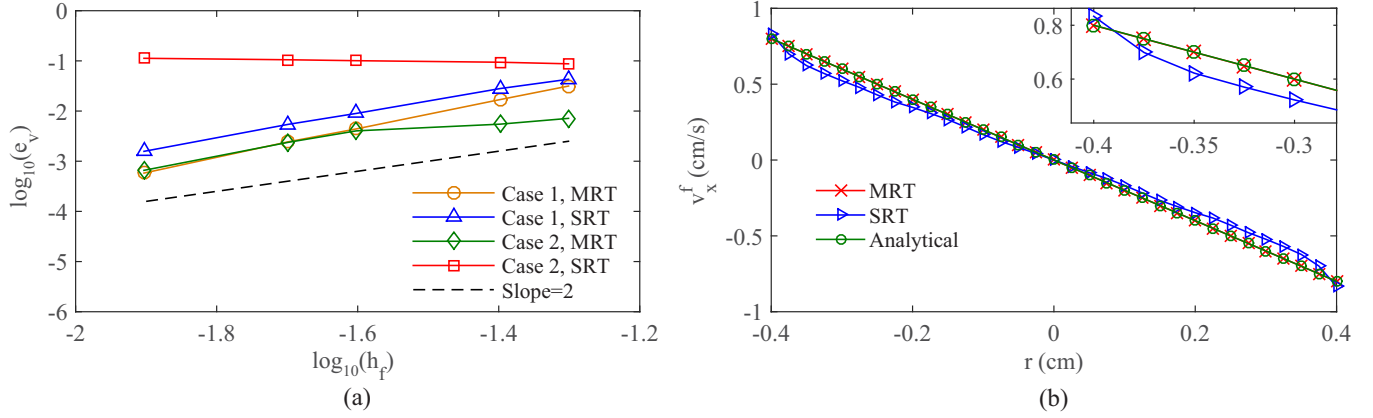
FIG. 5. (a) Spatial convergence properties of the fluid velocity. (b) Tangential velocity profiles alone the line $\theta = 0$.

analytical solution with the SRT model in case 2. As pointed out by Le and Zhang [25] and Lu *et al.* [26], the abnormal fluid velocity profiles and the numerical slip at the IB boundary layers appear if the relaxation time parameters are improperly chosen. In this numerical test, dimensionless kinetic viscosities in the LB calculation are $v_0^f = 0.001$ for case 1 and $v_0^f = 0.1$ for case 2. In all the numerical simulations in this paper, the dimensionless LB time step δt and lattice size δx are set to be equal. The corresponding relaxation time τ for different mesh sizes can be obtained by Eq. (12). As listed in Table I, for case 1, the relaxation time τ is smaller than 1; the numerical slip is not obvious. But in case 2, with the LB mesh getting smaller, τ becomes larger. The results obtained by SRT deteriorate badly and those from the MRT still appear good, which is consistent with Le and Zhang's [25] and Lu *et al.*'s [26] results. This also shows that the accuracy of the present method is significantly improved by employing the MRT-based LB model compared with the original IB-LBM coupling S-PIM scheme [27], in which the SRT-based LB framework is used.

B. Beam in a fluid tunnel

In this section, a classical static state FSI problem, a beam deformation problem in a fluid tunnel, is simulated. The accuracy to enforce the nonslip boundary conditions at the immersed boundary points, the computational efficiency, and the robustness in the range of solid stiffness of the present method are discussed. The sketch of this problem is shown in Fig. 6. In the problem, the deformation of a beam with its bottom fixed in a tunnel filled with viscous fluid is considered.

TABLE I. The relaxation time parameter τ for different sets of meshes for the simulation of cylindrical Couette flow.

h_f (cm)	τ (Case 1)	τ (Case 2)
1/20	0.54	4.5
1/25	0.55	5.5
1/40	0.58	8.5
1/50	0.60	10.5
1/80	0.66	16.5

The length of the beam is $b = 0.8$ cm and the thickness of the beam is $a = 0.04$ cm. The length of the tunnel is $L = 4.0$ cm and the height of the tunnel is $H = 1.0$ cm. The viscosity μ^f and density ρ^f of the fluid are chosen to be 0.1 g/(cms) and 1 g/cm^3, respectively. At $t = 0$, both solid and fluid are at rest and the gravity is ignored. The boundary conditions for the fluid domain are set as follows:

$$\text{inlet: } v_x = 1.5(-y^2 + 2y) \text{ (cm/s)}, v_y = 0;$$
$$\text{outlet: } \rho^f = \rho_0;$$
$$\text{upper boundary: } v^y = 0;$$
$$\text{bottom boundary: } v^x = v^y = 0. \quad (47)$$

The nonequilibrium extrapolation method [38] is employed to implement the boundary conditions except on the beam surface. Both rigid and elastic beam cases are considered in the simulation. The scaling factors in this numerical test are set as

$$C_l = 1 \text{ cm}; \quad C_t = 0.1 \text{ s}; \quad C_\rho = 1 \text{ g/cm}^3. \quad (48)$$

1. Rigid beam

In this case, the beam is rigid which means the solid boundary velocity and the displacement always remain zero. Three methods—the direct-forcing IB-LBM [17], the bounce-back based LBM, and the present method—are employed for the simulation. The direct-forcing scheme here can be seen as a reduction version of the present method if we set the force correction coefficient k to be 1. The bounce-back method here is used to get benchmark results for comparison considering that the method is more suitable for such problem with static rigid boundary conditions. Three different mesh sizes—MS1, $h_f = 1/50$ cm, $h_s = 1/50$ cm; MS2,
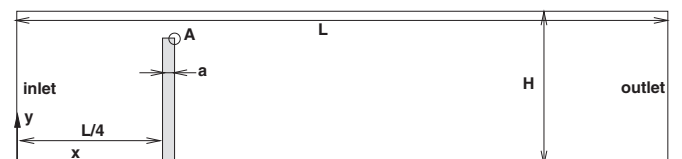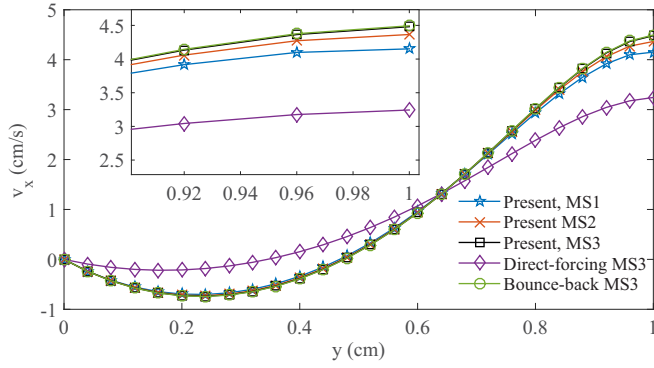

FIG. 6. Sketch of a beam in a fluid tunnel.

FIG. 7. Comparison of horizontal fluid velocities along the vertical plane $x = 2$ cm using the direct-forcing IB-LBM [17], the bounce-back based LBM, and the present IB-LBM. Three mesh sizes $h_f = 1/50$ cm, $1/100$ cm, $1/200$ cm are employed using the present method. The results by the direct-forcing IB-LBM and bounce-back based LBM are obtained on the finest mesh size.

$h_f = 1/100$ cm, $h_s = 1/100$ cm; MS3, $h_f = 1/200$ cm, $h_s = 1/200$ cm—are employed for the present method. The results obtained by the direct-forcing and the bounce-back method are on the finest mesh grid M3.

First, the horizontal fluid velocities are investigated along the vertical plane $x = 2$ cm which corresponds to the plane $x = L/2$ as plotted in Fig. 7. As shown, the results obtained by the present method are precisely consistent with those obtained by the bounce-back method. However, the results from

the direct-forcing method show significant errors, and they even cannot compete with those with the present method using the coarsest mesh MS1. We further investigate the horizontal velocity contours and the streamlines near the beam, which is shown in Fig. 8. As we can see, the present method and the bounce-back method get almost the same results. The horizontal velocity contours show a similar pattern outside the beam. The velocities inside the beam are shown to be zero. No streamlines can be found to penetrate into the beam obtained by both methods. The results show that the nonslip boundary conditions can be well enforced at the IB points by employing the force correction technique. However, as shown in Figs. 8(c)–8(d), the results from the conventional direct-forcing method without using the force correction technique largely deviate from those from the present method and bounce-back one. The horizontal velocities inside the beam become nonzero and the unphysical phenomenon of the streamline penetration happens. Quantitatively, the boundary velocity error e_b is investigated. e_b is defined as

$$e_b = \frac{1}{N_b} \sqrt{\sum_{n=1}^{N_b} \frac{(\mathbf{U}^f - \mathbf{U}^s)}{U_0^2}}, \tag{49}$$

where N_b is the number of the immersed-boundary points. $\mathbf{U}^f$ and $\mathbf{U}^s$ refer to the fluid velocity and solid velocity at the immersed-boundary points, respectively. U_0 is the maximum inlet fluid velocity, which is equal to 1.5 cm/s. As Table II shows, the boundary velocity error obtained by the present method is much smaller than the conventional direct-forcing
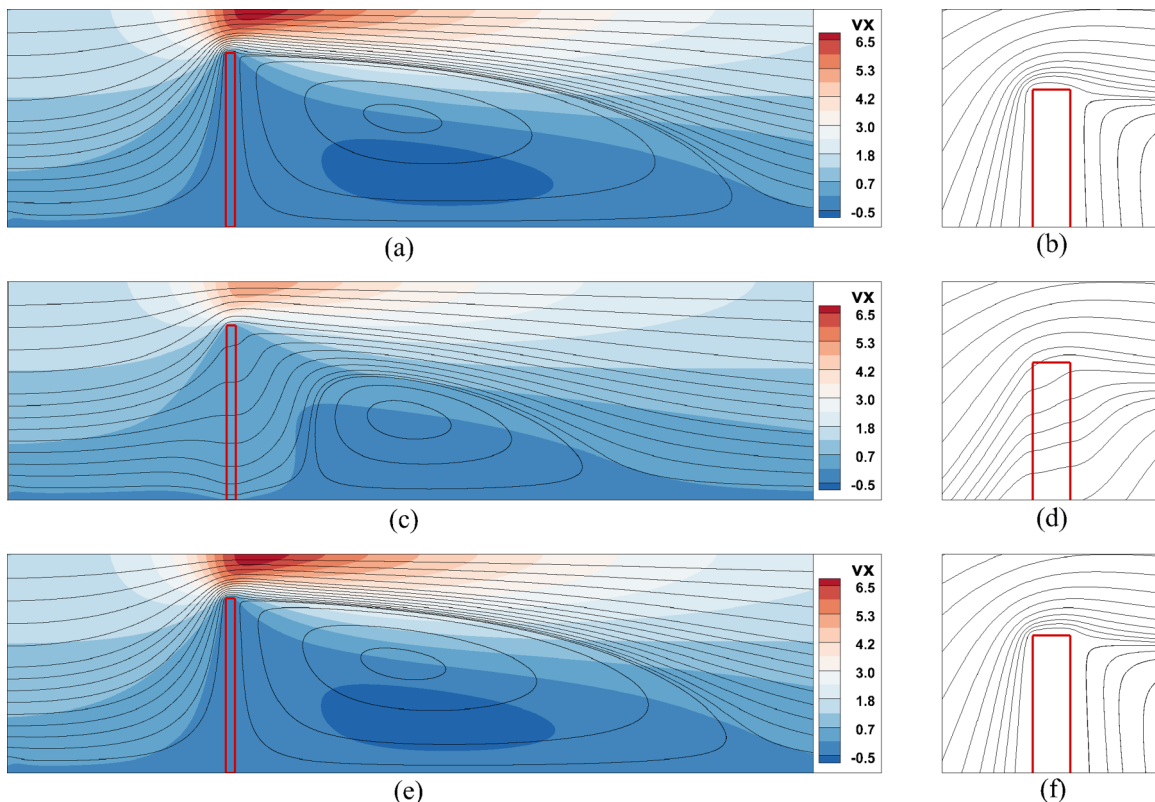

FIG. 8. Comparison of streamlines for flows over a rigid beam using the present IB-LBM [(a), (b)], the direct-forcing IB-LBM [17] [(c), (d)], and the bounce-back based LBM [(e), (f)].

TABLE II. The boundary velocity error e_b at the boundary of the rigid beam obtained by the present method and the direct-forcing method [17] with different mesh sizes.

	MS1	MS2	MS3
Present	0.5%	0.19%	0.09%
Direct forcing	2.12%	1.52%	1.07%

method, which indicates that the nonslip boundary condition is better enforced owing to the force correction technique. In addition, it is shown that the improvement becomes more significant as the mesh becomes finer. This explains why the error of the fluid velocity obtained by the direct-forcing method is so significant as shown in Fig. 7, while the results obtained by the present method are shown to be more accurate.

2. Elastic beam

An elastic beam is considered in this case. The parameters for the properties of the beam are set as $\rho^s = 7.8$ g/cm^3, $E^s = 1 \times 10^5$ g/(cms^2), $v^s = 0.3$.

The numerical results are first compared with those obtained by the immersed smoothed finite element method (IS-FEM) in Zhang *et al.*'s work [39]. Three different mesh sizes of $h_f = h_s = 1/50$ cm, $h_f = h_s = 1/100$ cm, and $h_f = h_s = 1/200$ cm are employed. Figure 9 shows the comparison results of the displacement at the beam tip point A against time. As shown in Fig. 9, good agreement is achieved between the results by the two methods. As can be seen, as the time increases, the beam begins to bend owing to the force from the fluid flow becoming larger and larger. As a result, the displacement at the beam tip point A increases gradually. At the time $t = 6$ s, the displacement reaches a constant value of about 0.478 cm because of the force balance of the fluid flow force and the bending force inside the beam. The final displacement values are coincident obtained by the two methods. However, small differences can be observed, which may caused by the different boundary condition treatments of the present method and the IS-FEM approach [39].

To test the convergence properties of the present method for such large deformation involved FSI problems, four different sets of mesh sizes, which are MS1, $h_f = 1/20$ cm, $h_s = 1/20$ cm; MS2, $h_f = 1/40$ cm, $h_s = 1/40$ cm; MS3,

FIG. 10. The convergence properties of the beam tip displacement and fluid velocity at $t = 10$ s.

$h_f = 1/50$ cm, $h_s = 1/50$ cm; MS4, $h_f = 1/100$ cm, $h_s = 1/100$ cm, are chosen to simulate this numerical test. The results obtained by our finest mesh size of $h_f = h_s = 1/200$ cm are employed as the reference solution. The errors are obtained as follows:

Tip displacement error: $e_s = \left| \left(u_{xA}^{num} - u_{xA}^{ref} \right) / u_{xA}^{ref} \right|$;

Horizontal velocity error: $e_f = \left\| v_x^{num} - v_x^{ref} \right\|_{L2} / \left\| v_x^{ref} \right\|_{L2}$;

$$(50)$$

where u_{xA} and v_x are the component of tip point displacement and the fluid velocity at $x = 2.0$ cm in the x direction, respectively. The superscripts *num* and *ref* mean the numerical and the reference solutions. The spatial convergence properties of the present method are shown in Fig. 10. It can be observed that the second-order accuracy can be achieved for both solid displacement and fluid velocity. Furthermore, the streamlines
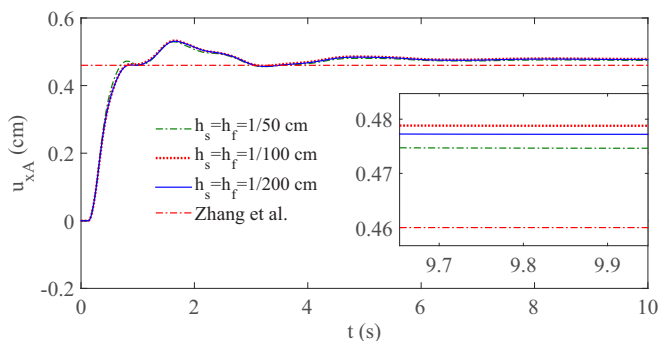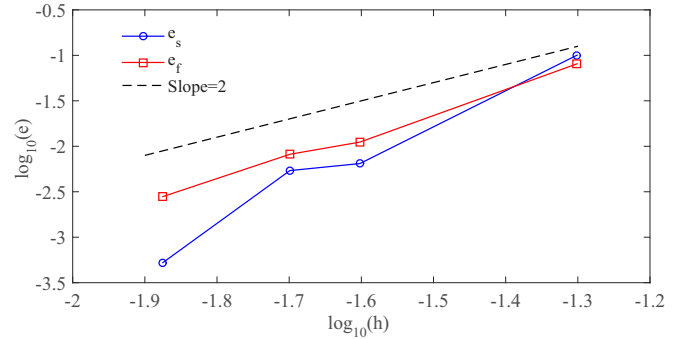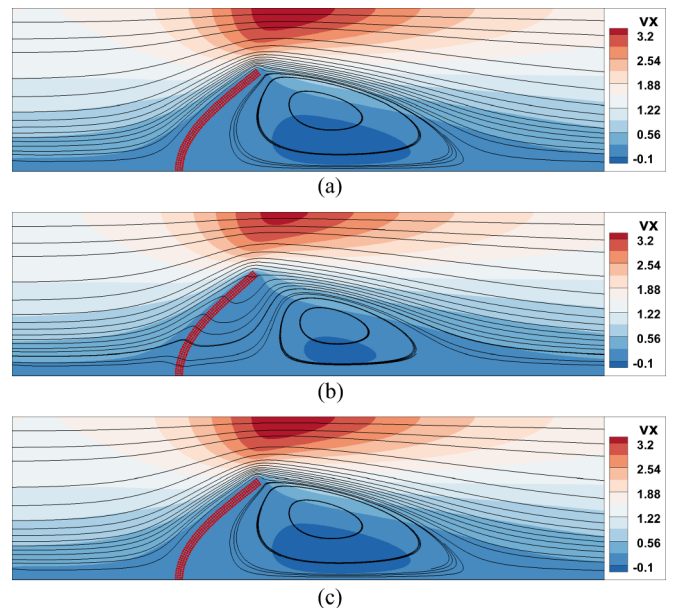

FIG. 9. Comparison of the tip displacement employing the present method with Zhang's results [39].

FIG. 11. The horizontal velocity contours and the streamlines snapshots at $t = 10$ s. The red dots represent the solid node positions. Results in (a), (b), and (c) are obtained by the present IB-LBM, the direct-forcing IB-LBM, and the implicit IB-LBM, respectively, with the same mesh size of $h_s = 1/75$ cm, $h_f = 1/100$ cm.

TABLE III. The boundary velocity error e_b at the boundary of the elastic beam obtained by the present method and the direct-forcing method [17] with different mesh sizes.

	MS1	MS2	MS3
Present	0.17%	0.06%	0.03%
Direct forcing	0.73%	0.51%	0.35%

TABLE V. Comparison of the robustness of the present coupling scheme for the cases with and without the time-average technique. ✓ means that the simulation is stable until $t = 10s$. × means that the simulation blows up before $t = 10$ s.

	E^s [g/(cms^2)]					
	Rigid	1×10^9	1×10^7	1×10^5	1×10^4	1×10^3
Present	✓	✓	✓	✓	✓	×
Conventional	✓	×	×	×	×	×

near the solid boundary at $t = 10$ s obtained by the present IB-LBM, the implicit IB-LBM [16], and the direct-forcing IB-LBM [17] are investigated as plotted in Fig. 11. As shown in Fig. 11, the horizontal velocity contours of the present method and the implicit method are almost the same. The streamlines penetration problem is avoided in the present method and the implicit method, while in the results obtained by the direct-forcing method, the streamlines penetrate through the solid surface which reveals that the nonslip boundary conditions are not guaranteed and it causes the extra errors in the simulation. And the flow patterns show deviation from those obtained by the implicit and the present method. Similarly to the analysis carried out in Sec. III B 1, the boundary velocity error e_b is also investigated quantitatively. As Table III shows, the boundary error is reduced significantly owing to the force correction technique and better performance is shown with the mesh getting finer. Thus it can be concluded that the force correction technique employed in the present IB-LBM scheme is crucial for the enforcement of the nonslip boundary conditions, along with the improvement of simulation accuracy.

To test the computational efficiency of the present method, the computational time and the tip displacement errors e_s are investigated. The implicit IB-LBM [16] and the direct-forcing IB-LBM [17] are also employed for this problem to make a comparison with different mesh sizes. All simulations are run on a computer of Intel Core i7-4790, CPU 3.60 GHz, RAM 8.0 G. The CPU time for the implementation of the whole algorithm is counted as t_{CPU} until it comes to the physical time $t = 10$ s. Because the implicit method can accurately enforce the nonslip boundary condition, the result obtained by the implicit method is chosen as the reference solution. It should be pointed out that in the implicit method, the solid/fluid mesh ratio $\Delta h = h_s/h_f$ cannot be too small or it would lead to instability [18]. Thus the mesh size $h_s = 1/100$ cm,

$h_f = 1/200$ cm is chosen to obtain the reference solution. In addition, the estimated computational efficiency for each method is investigated as well, which is defined as efficiency $= 1/(e_s \times t_{CPU})$. Table IV shows the CPU time, the tip displacement error, and the computational efficiency of different IB-LBMs. It is shown that the present method has no more than 6% CPU time cost than the direct-forcing method, but at least 3.5 times less than that of the implicit method with the same mesh size. As for the accuracy, the present method is able to obtained much more accurate results compared with the direct-forcing method under the same conditions. And with the mesh getting finer, the present method is able to obtain comparable accuracy with the implicit method. In terms of the computational efficiency, the present method has the best performance compared with the other two IB-LBMs. It should be noted that the efficiency test in this paper is conducted for simple FSI problems; in actual implementation, when dealing with complex problems with a large number of boundary points, the advantage of the present method is more significant.

Finally, the robustness of the method with different solid stiffness and solid/fluid density ratio is investigated. First, the simulations for beams with a wide range of elasticity from very soft to very rigid type by choosing a different Young's modulus are carried out. The other parameters are set the same as that in the above. The mesh size of $h_f = h_s = 1/200$ cm is chosen. Except for the present coupling method, the conventional method, in which the boundary force is evaluated using Eq. (41), is also used to simulate this numerical test. As shown in Table V, the present coupling scheme is able to handle both the rigid solid and the elastic solid with a wide range of Young's modulus $[E^s = (1\times10^4 \sim 1\times10^9)$ g/(cms^2)].

TABLE IV. Comparison of the computational time t_{CPU}, the tip displacement errors e_s, and the computational efficiency employing the present IB-LBM, the direct-forcing IB-LBM [17], and the implicit [16] methods with different mesh sizes. The fluid size is chosen as $h_f = 1/100$ cm for all cases.

		h_s (cm) = 1/30	1/40	1/50	1/75	1/100
Present	t_{CPU} (s)	74	88	103	158	230
	e_s	0.0354	0.0211	0.0159	0.0062	0.0013
	efficiency	0.04	0.54	0.61	1.03	3.36
Direct forcing	t_{CPU} (s)	71	84	98	150	222
	e_s	0.0680	0.0589	0.0550	0.0434	0.0378
	efficiency	0.20	0.20	0.19	0.15	0.12
Implicit	t_{CPU} (s)	261	416	635	1200	
	e_s	0.0331	0.0178	0.0118	0.0025	unstable
	efficiency	0.12	0.14	0.13	0.34	

TABLE VI. Comparison of the robustness of the coupling schemes with different solid/fluid ratios λ. "Present" and "Conventional" denote the schemes with and without the time-average technique, respectively. $\checkmark$ means that the simulation is stable until $t = 10$ s. $\times$ means that the simulation blows up before $t = 10$ s.

		λ						
		1×10^{-3}	1×10^{-2}	1×10^{-1}	1	1×10^{1}	1×10^{2}	1×10^{3}
Present	Stability	$\times$	$\checkmark$	$\checkmark$	$\checkmark$	$\checkmark$	$\checkmark$	$\checkmark$
	δt_s (s)	1×10^{-7}	1×10^{-7}	1×10^{-6}	5×10^{-6}	2×10^{-5}	5×10^{-5}	1×10^{-4}
Conventional	Stability	$\times$	$\times$	$\times$	$\times$	$\times$	$\times$	$\checkmark$
	δt_s (s)	1×10^{-7}	1×10^{-7}	1×10^{-7}	1×10^{-7}	1×10^{-7}	1×10^{-7}	1×10^{-7}

However, it is found that the simulations blow up when using the conventional method even at a very early stage except for the rigid beam.

Furthermore, the simulation of a flexible beam with different solid/fluid density ratios λ is also carried out. The fluid density is fixed and a number of solid densities are chosen. The other parameters are set the same as that in the above. As Table VI shows, the present method is stable with a wide range of solid/fluid ratio ($0.01 \leqslant \lambda \leqslant 1000$) except for the case when $\lambda = 0.001$. Meanwhile, it is found that one has to choose smaller solid time step δt_s to ensure stability when λ decreases. As pointed out by Sotropoulos and Yang [40], numerical instabilities may happen for the loose coupling schemes when the structure density is close to or lighter than the density of the fluid and the FSI iteration scheme can converge as long as the time step is small enough. The results of this test is shown to be in accordance with Sotropoulos and Yang's [40] conclusions. In addition, the cases without time-average technique are also tested. It is shown that the simulation blows up when $\lambda \leqslant 100$ even with the small time step $\delta t_s = 1\times10^{-7}$. Note that the instability may be caused by the artificial energy generated at the fluid-solid interface and it will be specifically investigated in Sec. III C.

Illustrated by the test above, the time-average technique improves the robustness of the present method, which enables the present coupling scheme to be stable with various solid stiffness and solid/fluid density ratio.

C. A flexible beam in the wake of a cylinder

In this section, a flexible beam flapping in the wake of a cylinder is simulated to test the performance of the present method for this kind of unsteady FSI problem which is more challenging than the former ones. Turek and Hron [41] analyzed this problem in detail and the benchmark solutions are given in their work. Here we will investigate the efficiency of our method by comparing the results in the previous works. As shown in Fig. 12, the fluid domain of this problem is set as $L = 2.5$ m, $H = 0.41$ m. A circular cylinder with diameter
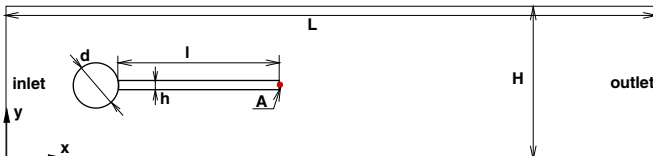

FIG. 12. Sketch of a flexible beam in the wake of a cylinder.

$d = 0.1$ m is placed at (0.2 m, 0.2 m). On the right surface of the cylinder, a flexible beam is fixed with its left head while its tail is free in the fluid. The length and the thickness of the beam are set to be $l = 0.35$ m, $h = 0.02$ m. The viscosity and density of the fluid are set to be $\nu^f = 1$ kg/(ms) and $\rho^f = 1\times10^3$ kg/m^3. The beam's related parameters are given as density $\rho^s = 1\times10^4$ kg/m^3, Young's modulus $E^s = 1.4\times10^6$ kg/(m s^2), Poisson's ratio $\nu^s = 0.4$. The cylinder is treated as a rigid body. The nonslip boundary conditions are applied at the upper and bottom boundaries of the computational fluid domain. For the outlet boundary, the fluid density is equal to ρ_0. The inlet velocity is set as

$$(v_x, v_y) = \begin{cases} \left(\bar{v}\frac{1-\cos(\pi t/2)}{2}, 0\right), & t < 2.0 \text{ s}, \\ (\bar{v}, 0), & t > 2.0 \text{ s}; \end{cases} \tag{51}$$

$\bar{v} = 6y(H - y)/H^2$ m/s is chosen, and thus the Reynolds number is Re = 100. The fluid boundary conditions are implemented by the nonequilibrium extrapolation method [38]. At $t = 0$, the fluid and solid are at rest and the fluid density $\rho^f = \rho_0^f$. The scaling factors in this numerical test are set as

$$C_l = 1 \text{ m}; \quad C_t = 0.1 \text{ s}; \quad C_\rho = 1000 \text{ kg/m}^3. \tag{52}$$

Several typical snapshots of the velocity contour and the pressure contour in an oscillating cycle are plotted in Fig. 13 and Fig. 14. As shown in Fig. 13, the vortices shed from the upper side and the lower side of the cylinder interact with each other after passing the end point of the beam, which gives rise to a von Kármán vortex street. The oscillating motion of the beam produces a regular vortex pattern that is advected along the channel. Furthermore, as shown in Fig. 14, a high pressure zone can be observed on the leading side of the cylinder, which is created by the impingement of the flow on the cylinder surface. At $t = 0T$, the beam is at the uppermost position and the flow is obstructed on the upper surface of the beam near the end point, resulting in the development of a high pressure zone and a corresponding low pressure zone at the upper side and the lower side of the beam, respectively. Then the beam is forced to move downward and results in the neutralization of the pressure. As the beam approaches the horizontal position, it continues to move downward due to its inertia. In the meantime, a high pressure zone starts to develop on the lower side of the beam and finally the beam is stopped once the pressure value increases to a threshold value at $t = T/2$. After this time point, the beam would move up and undergo the complete reversal motion. Figure 15 shows
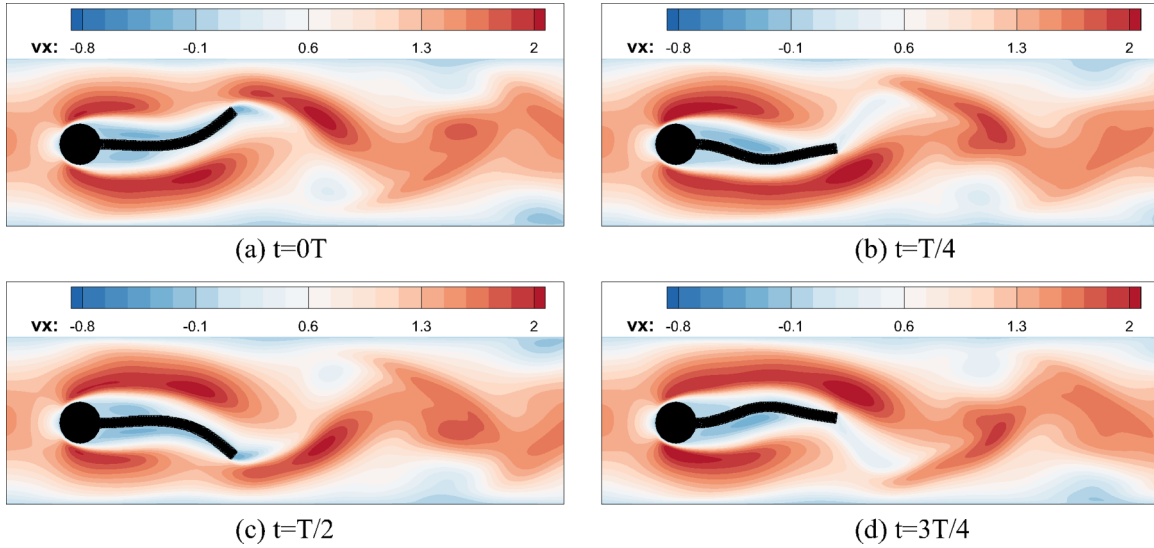
FIG. 13. The horizontal velocity contours at four typical time shots in an oscillating cycle. T denotes the oscillating period.

the displacement of the tail point A in the x and y directions. It is illustrated that after about 9 s, the system settles into a large-amplitude self-excited oscillation and the tail displacement of the flag changes periodically. All the phenomena observed here agree well with those from the previous work [42].

In order to make further comparison with the previous works [41–43] quantitatively, the mean value and amplitude of the tail displacement are employed which are defined as

$$u_{\text{ave}} = (u_{\text{max}} + u_{\text{min}})/2, \quad u_{\text{amp}} = (u_{\text{max}} - u_{\text{min}})/2, \quad (53)$$

where u_{max} and u_{min} are the maximum and minimum of the tail displacement, respectively. Four different mesh sizes are chosen, which are MS1: $h_f = 1/500$ m, $h_s = 1.5/500$ m; MS2: $h_f = 1/700$ m, $h_s = 1.5/700$ m; MS3: $h_f = 1/1000$ m, $h_s = 1.5/1000$ m; MS4: $h_f = 1/2000$ m, $h_s = 2/2000$ m. Table VII shows the mean value and amplitude of the tail point A obtained by the present method. Meanwhile, the results from the previous works are also listed to make

comparison. It can be seen that the results of the present method agree well with the reference solutions. In addition, the temporal evolution of the beam tip is compared with the benchmark results in Turek *et al.*'s work [41]. As Fig. 16 shows, the history curves of the tip displacements u_y and u_x are shown to deviate from the reference solutions. With the mesh getting finer, u_x and u_y converge to Turek *et al.*'s results [41] and good agreements are achieved with MS4.

A convergence study for this transient case is carried out and the results obtained with the finest mesh size are employed as the reference solutions. As shown in Fig. 17, the slopes for $u_{x,\text{amp}}$, $u_{y,\text{amp}}$, $u_{x,\text{ave}}$, and $u_{y,\text{ave}}$ are 1.37, 1.58, 1.22, and 2.81, respectively. For such transient FSI problems, the convergence rate of the results may reduce to the first order, which is due to the dual time step used in the present scheme. However, the orders of the accuracy obtained from the output variables are greater than 1, which is satisfactory for an immersed-boundary method [44].
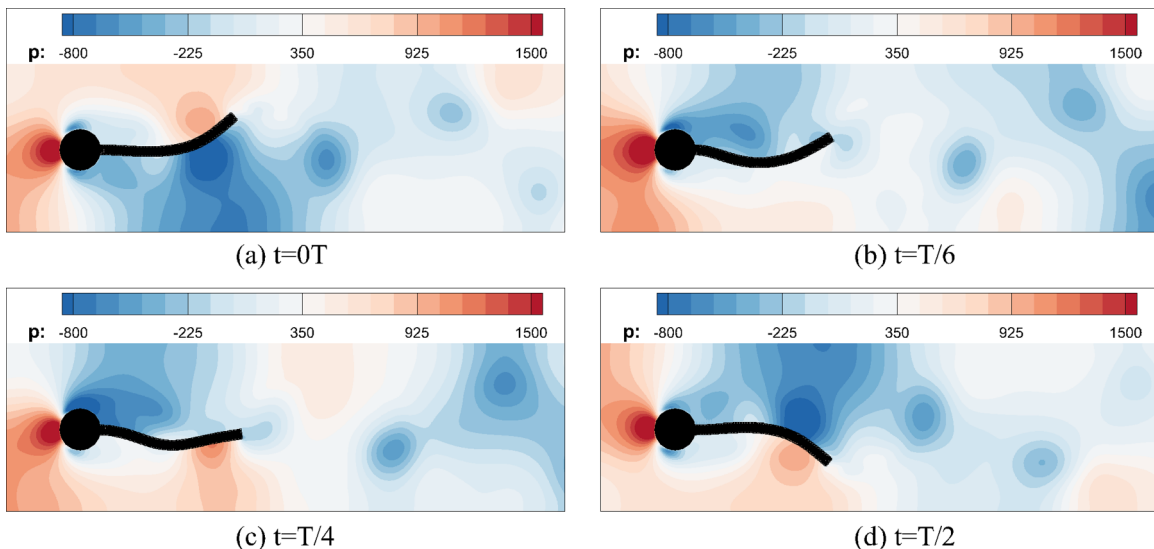

FIG. 14. The pressure contours at four typical time shots in an oscillating cycle. T denotes the oscillating period.
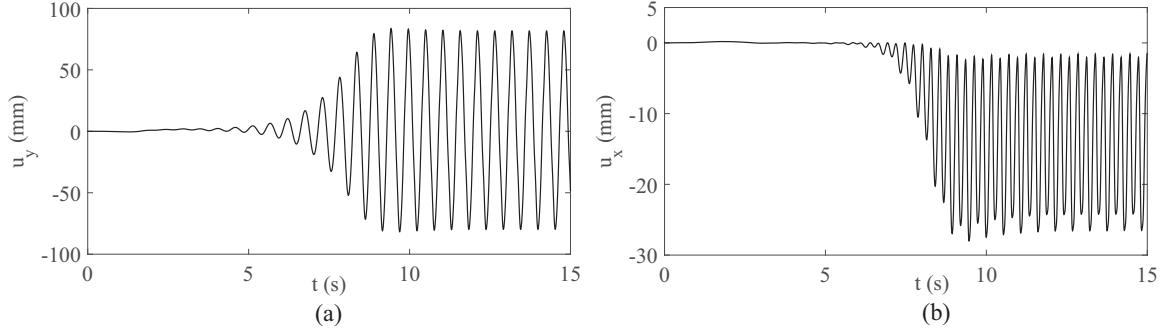
FIG. 15. (a) The displacement in the y direction of point A. (b) The displacement in the x direction of point A.

Furthermore, the conservation of energy at the interface is an important issue for stability. The time-average procedure employed in the present work is able to reduce the generation of artificial interface energy effectively, which improves the stability of the present coupling scheme. The analysis of this issue is carried out similarly to Kollmannsberger *et al.*'s work [3].

The artificial energy $\Delta\mathbf{E}_T$ is calculated as [3]

$$\Delta\mathbf{E}_T = \int_\Gamma \int_{t_n}^{t_n+\delta t_f} (\mathbf{T}^f\mathbf{v}^f + \mathbf{T}^s\mathbf{v}^s)\,dt\,d\Gamma, \qquad (54)$$

where Γ represents the immersed-boundary curve. $\mathbf{T}^f$ and $\mathbf{T}^s$ are the traction vector of the fluid and solid at the immersed boundaries. $\mathbf{v}^f$ and $\mathbf{v}^s$ are fluid and solid velocities at the immersed boundaries. Note that several subcycles are carried out within one fluid step in the present dual time stepping approach; the evaluation of $\Delta\mathbf{E}_T$ from fluid step n to $n+1$ can be specifically written as

$$\Delta\mathbf{E}_T^{n\to n+1} = \int_\Gamma \left[\mathbf{T}_{n+1}^f\mathbf{v}_{n+1}^f + \sum_{i=1}^{n_0}\left(\mathbf{T}_{n+i/n_0}^s\mathbf{v}_{n+i/n_0}^s\right)\right]d\Gamma, \quad (55)$$

where n_0 is the number of subcycles. In addition, the total artificial energy $\mathbf{E}_{\text{total}}$ is also considered. $\mathbf{E}_{\text{total}}$ is obtained through a summation of the $\Delta\mathbf{E}_T$ from the starting step $n=1$

to the current time step n_{current}, which can be written as

$$\mathbf{E}_{\text{total}} = \sum_{n=1}^{n_{\text{current}}} \Delta\mathbf{E}_T^{n\to n+1}. \qquad (56)$$

The transient case in this section is employed to carry out the analysis of the artificial energy effect. The mesh size is set as $h_s = 1.5h_f = 1/500$ cm. Figure 18 shows the time history of instantaneous and total artificial energy. The superscripts a and b denote the results obtained with and without employing the time-average technique, respectively. It can be clearly observed that the artificial energy increases rapidly and instability occurs at $t \approx 0.4$ s without the time-average technique. However, $\Delta\mathbf{E}_T$ and $\mathbf{E}_{\text{total}}$ remain within acceptable bounds when employing the time-average technique. The analysis illustrates that the time-average procedure is able to reduce the artificial energy at the immersed boundary interface, which improves the robustness for the present method.

D. Swimming of a self-propelled fishlike body

In the end, a two-dimensional self-propelled fishlike swimming problem is simulated to demonstrate the capacity of the present method to the problems combining strong fluid-solid interactions and large solid deformations. In this problem, the fish body deforms in response to the fluid force and the muscle force. In the meantime it affects the fluid flow around. Much
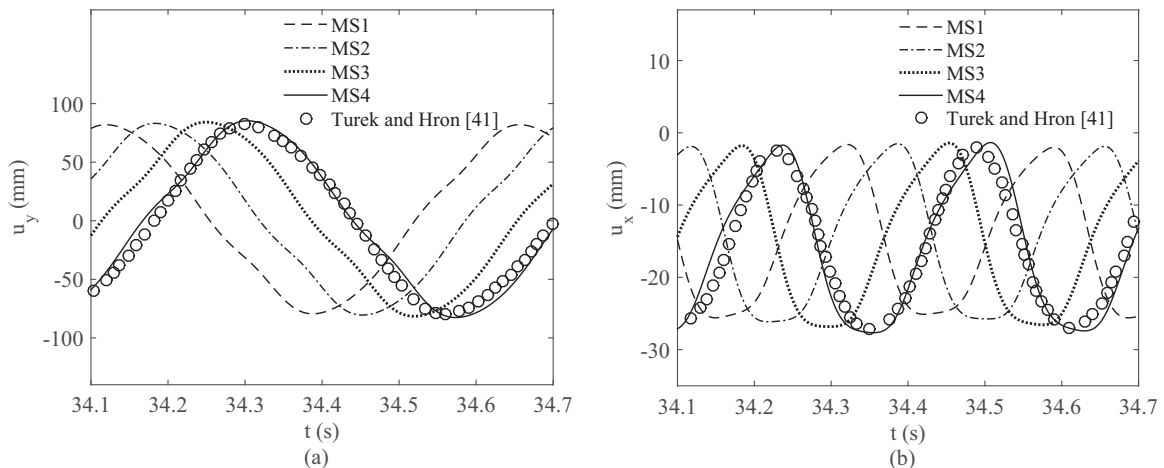

FIG. 16. The temporal evolution of the beam tip with different mesh sizes: (a) tip displacement in the y direction; (b) tip displacement in the x direction.

TABLE VII. The mean value and amplitude of the tail point A in the x and y directions obtained by the present method with different mesh sizes and in the previous works.

	$u_{y,\text{ave}}$ (mm)	$u_{y,\text{amp}}$ (mm)	$u_{x,\text{ave}}$ (mm)	$u_{x,\text{amp}}$ (mm)
Present, MS1	1.27	80.72	−13.61	11.99
Present, MS2	1.31	81.82	−13.83	12.32
Present, MS3	1.33	82.87	−14.12	12.70
Present, MS4	1.34	83.95	−14.50	13.15
Turek and Hron [41]	1.23	80.6	−14.58	12.44
Nordanger *et al.* [42]	1.30	81.043	−14.710	12.743
Zhang *et al.* [43]	1.0	83.0		

progress has been made to study this problem numerically [45–53], but in most previous works, the motion of the fish body is prescribed. In this paper, the fishlike body is self-propelled which means the muscle force is given to generate the movement responses of the fish body. The pushing force of the fish comes from the resulting FSI force acting on the fish body surface. Muscle force and body stiffness with different values and their effects on the straight-line fishlike swimming speed are discussed.

Following the previous work [52], the NACA0012 airfoil is employed to represent the fish body. As shown in Fig. 19, the length of the fish is 1 m and it is divided into three parts: the head part ($0 \sim 0.2L$), the muscle part ($0.2L \sim 0.88L$), and the tail part ($0.88L \sim 1.0L$). To ensure the straight-line swimming, the head part is restrained by adding an elastic constraint force in the y direction as

$$\mathbf{F}_{\text{head}}(\mathbf{X}, t) = -K_s[\mathbf{X}(t) - \mathbf{X}_0]\mathbf{n}_y, \quad \text{with } \mathbf{n}_y = (0, 1), \quad (57)$$

where $\mathbf{X}_0$ is chosen as $\mathbf{X}_0 = (0, 0)$. K_s is set to be 1×10^6 N/m. The muscle force is simplified by adding a surface force term on the fish's muscle part, which results in a periodic flapping motion, and it can be expressed as follows:

$$\mathbf{F}_{\text{body}}(m, t) = F_s \sin[\pi(x - 0.2L)]\mathbf{n}_s,$$
$$\text{if } y_A > ld, \quad \mathbf{n}_s = (0, -1); \quad (58)$$
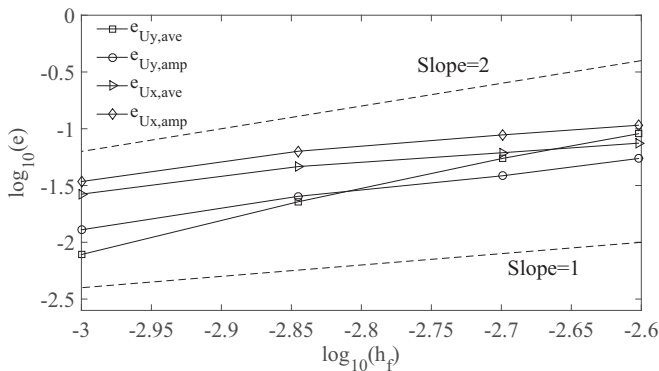$$\text{if } y_A < -ld, \quad \mathbf{n}_s = (0, 1).$$

FIG. 17. The convergence properties of the mean value and amplitude of the beam tail point A in the x and y directions. The results from Turek and Hron [41] are employed as the reference solutions.
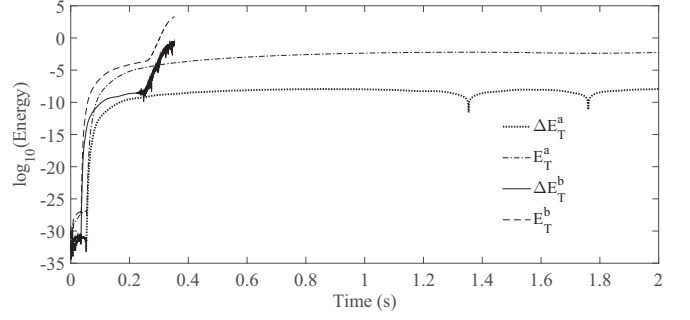

FIG. 18. The time history of instantaneous and total artificial energy. The superscripts a and b denote the results obtained with and without employing the time-average technique, respectively.

Initially, the muscle force is at the direction of $\mathbf{n}_s = (0, 1)$. No extra muscle force is exerted on the tail part. The fluid properties are set as follows: kinematic viscosity $\nu_f = 0.01$ m^2/s, density $\rho_f = 1 \times 10^3$ kg/m^3. The solid parameters are chosen as density $\rho_s = 1 \times 10^3$ kg/m^3, Poisson ratio $\nu_s = 0.3$. The general periodic boundary conditions are employed for all the outer boundaries. The scaling factors in this numerical test are set as

$$C_l = 1 \text{ m}, \quad C_t = 0.01 \text{ s}, \quad C_\rho = 1000 \text{ kg/m}^3. \quad (59)$$

First, we test the problem with two fluid domain sizes: $8L \times 4L$ and $16L \times 8L$. The fish's head is initially at $(6L, 2L)$ and $(12L, 4L)$, respectively. The muscle strength and the body stiffness are set as $F_s = 1 \times 10^4$ N/m^2, $E^s = 1 \times 10^7$ kg/(ms). The curves of the swimming speed against time at the x direction obtained by the two different fluid domain sizes are shown in Fig. 20. From 0 to 2 s, the fish experiences the acceleration process. After $t = 2$ s, the fish's speed reaches a steady periodic state. Meanwhile, the speed is periodically fluctuant, which is mainly due to the swing of the tail. Qualitatively, the fishlike swimming patterns in the present work are in accordance with those in the previous works [50,52], even though there are some differences in the modeling of the fish body. It is also found that the difference of the mean fish swimming speed from $t = 2$ s to $t = 6$ s simulated by the two fluid domains is 1.95%. Considering the computational cost, the fluid domain size of $8L \times 4L$ is chosen in the following simulations.

Next we investigate the flow field, the FSI force exerted on the fish, and the corresponding swimming speed. Figure 21 shows the fluid motion around the fish at four typical time stages, in which the muscle strength and the body stiffness are set as $F_s = 1 \times 10^4$ N/m^2, $E^s = 5 \times 10^6$ kg/(ms). Each time the tail reverses direction, a strong single vortex is shed. Multiple
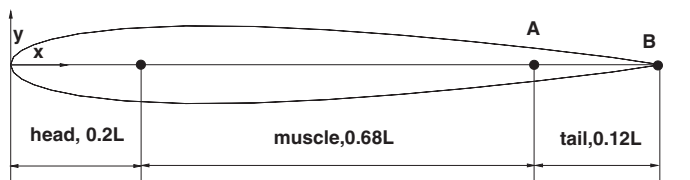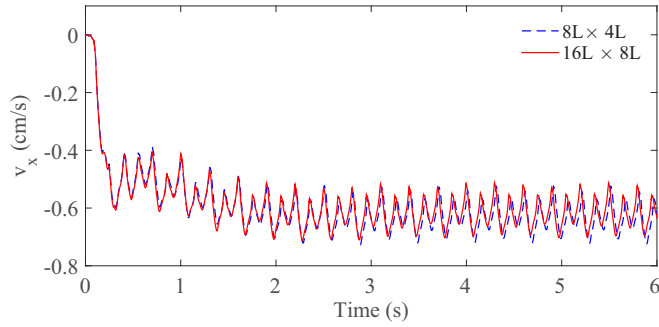

FIG. 19. Model of the fish.

FIG. 20. Swimming speed against time in the x direction.

weak secondary vortices are also produced from the fish head and finally at the tail. At $t = 4.33$ s and 4.47 s, the fish's tail part moves away from the axis of the body and the body becomes the S shape. At $t = 4.42$ s and 4.60 s, the fish's tail part moves close to the axis of the body and the body becomes the C shape. The periodic change of the fish body shape corresponds to different motion states. Figure 22 shows the displacement of the tail point B at the y direction d_{yB}, total FSI force F_x at the x direction, and swimming speed v_x against time at the steady periodic state. It is illustrated that the cycle time of d_{yB} is twice that of F_x. We divide the one cycle of d_{yB} into four stages: $T1$, $T2$, $T3$, and $T4$. In $T1$, the fish tail moves up from the axial line. In $T2$ and $T3$, the tail goes down from the top position. The fish tail goes up and back to the axis line again in $T4$. It can be observed that in $T1$ and $T3$, the fish tail moves away from the axis line and the fish body presents the S shape. The fish gains the pushing FSI force and enters into an accelerated motion. In $T2$ and $T4$, the tail is moving back to the axis line and the fish body presents the C shape. The FSI force exerted on the fish surface acts as the resistance and the fish experiences the deceleration motion. The phenomena analyzed above are consistent with those given in Ref. [52].

The body stiffness also affects the mean steady swimming speed of the fish. The effect of the body stiffness is also investigated quantitatively. Several types of self-propelled
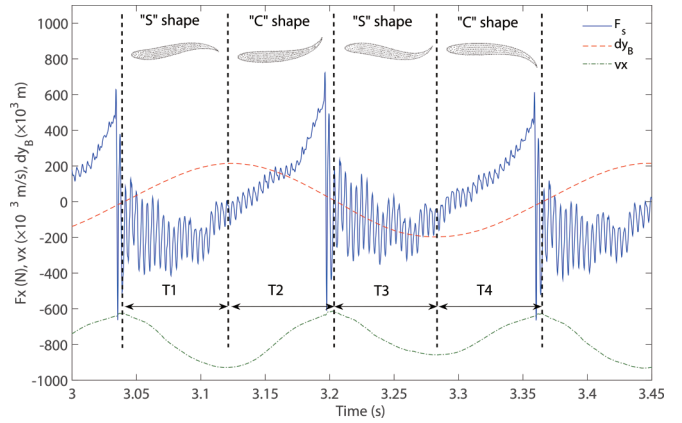

FIG. 22. Tail displacement d_{yB}, total FSI force F_x, and swimming speed v_x against time in the x direction.

fish with different E^s and F_s are simulated. The results are shown in Fig. 23. It can be observed that with the same muscle strength F_s, there exists an optimal Young's modulus E_o^s for the maximum steady speed. And E_o^s increases with the muscle strength F_s. The optimal muscle strength–stiffness schemes approximately are $(F_s \text{ (N/m)}, E^s \text{ [kg/(ms)]}) = (1.5 \times 10^4, 1.0 \times 10^7), (1.0 \times 10^4, 5.0 \times 10^6), (5 \times 10^3, 1.0 \times 10^6)$. The results obtained by the present method are in accordance with those in Tytell *et al.*'s work [50], who pointed out that for a given muscle activation pattern, there are different optimal stiffness values for the fish's steady swimming speed. Meanwhile, it should be pointed out that in nature the motions of the fish are far more complicated than the straight-line swimming case simulated in this simulation. However, all these results to some extent reflect the mechanism of the fishlike swimming and clearly demonstrate the efficiency of the present method handling problems with strong FSI and large solid deformation. It is believed that the present method is still valid if suitable active control model is introduced to describe the fish swimming problem with more complex motions [48,49].

(a) t=4.33s

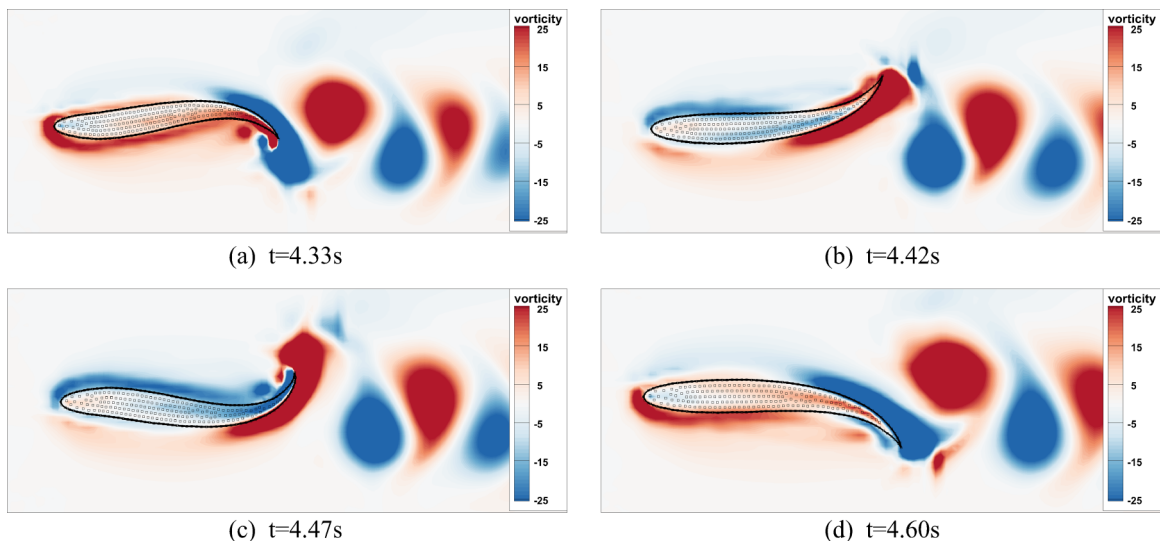(b) t=4.42s

(c) t=4.47s

(d) t=4.60s
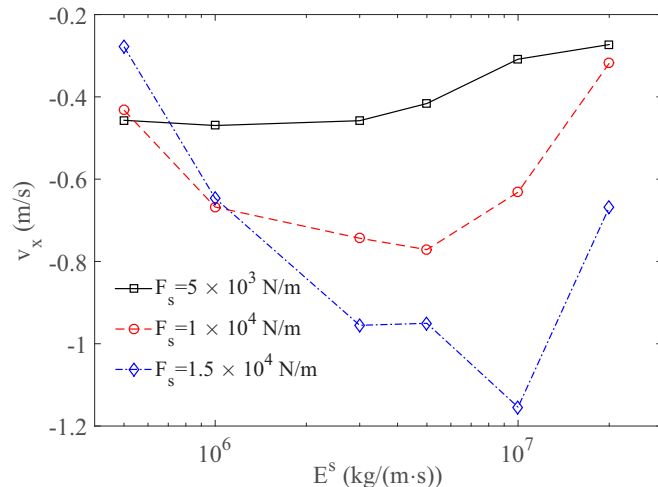
FIG. 21. Vorticity contours at four typical time stages.

FIG. 23. Swimming speed v_x against fish stiffness E^s with different muscle strength F_s.

In summary, the superiority of the present method is illustrated by several numerical tests. Compared with the original IB-LBM coupling S-PIM scheme [27], the nonslip boundary condition is much better enforced owing to the force correction technique employed in the present method, and the viscosity dependence is dramatically reduced by employing the MRT-based LB model. In addition, the present method is able to model realistic solids with large deformation rather than the fiber-like structure in the original force-correction-based IB-LB scheme [19]. Moreover, the robustness of the present method is much improved by adopting the time-average technique.

IV. CONCLUSIONS

In this paper, an immersed-boundary lattice Boltzmann method is proposed for large deformable solid involved FSI problems. The improvements that have been made in the method are clearly presented. And the efficiency of the method compared with previous ones is analyzed and validated by several numerical tests, including a simple FSI problem with analytical solution, a static state problem involving large solid deformation, and complex ones with unsteady state or strong fluid-solid interaction and large solid deformation combined. Some main conclusions can be drawn as follows:

(1) By modeling the solid domain based on the nonlinear constitutive law using the S-PIM, the present IB-LBM can deal with realistic solid deformation. In addition, the time-average technique is introduced which can reduce the artificial interface energy and enhance the robustness of the present scheme.

(2) The nonslip boundary conditions at the immersed boundaries can be much better enforced owing to the force correction technique adopted in the present IB-LBM. Moreover, the viscosity dependence is dramatically reduced by employing the MRT-based LB model.

(3) According to the numerical results, the efficiency of the present method is verified in terms of the boundary condition enforcement accuracy, the computational cost, the coupling robustness, and the capacity for complex problems. It is shown that the present method can handle the FSI problems with a wide range of solid stiffness and solid/fluid density ratio.

However, the numerical tests are limited to the two-dimensional case and the active control of the fish body motion is not considered in the present solid model, which are the objectives of future research.

[1] C. S. Peskin, J. Comput. Phys. **25**, 220 (1977).

[2] F. B. Tian, H. Luo, L. D. Zhu, J. C. Liao, and X. Y. Lu, J. Comput. Phys. **230**, 7266 (2011).

[3] S. Kollmannsberger, S. Geller, A. Düster, J. Tölke, C. Sorger, M. Krafczyk, and E. Rank, Int. J. Numer. Methods Eng. **79**, 817 (2010).

[4] J. Mohd-Yusof, CTR Annual Research Briefs, NASA Ames/ Stanford University, 1997, pp. 317–327.

[5] Y. H. Tseng and J. H. Ferziger, J. Comput. Phys. **192**, 593 (2003).

[6] Z. G. Feng and E. E. Michaelides, J. Comput. Phys. **195**, 602 (2004).

[7] T. Kürger, F. Varnik, and D. Raabe, Comput. Math. Appl. **61**, 3485 (2011).

[8] A. D. Rosis, S. Ubertini, and F. Ubertini, J. Fluids Struct. **45**, 202 (2014).

[9] A. D. Rosis, G. Falcucci, S. Ubertini, and F. Ubertini, J. Fluids Struct. **49**, 516 (2014).

[10] B. Dorschner, S. S. Chikatamarla, and I. V. Karlin, Phys. Rev. E **97**, 023305 (2018).

[11] C. Jiang, J. Yao, Z. Zhang, G. Gao, and G. Liu, Comput. Methods Appl. Mech. Eng. **340**, 24 (2018).

[12] S. Y. Chen and G. D. Doolen, Annu. Rev. Fluid Mech. **30**, 329 (1998).

[13] C. K. Aidun and J. R. Clausen, Annu. Rev. Fluid Mech. **42**, 439 (2010).

[14] Y. Kim and C. S. Peskin, Phys. Fluids **19**, 053103 (2007).

[15] H. Z. Yuan, X. D. Niu, S. Shu, M. J. Li, and H. Yamaguchi, Comput. Math. Appl. **67**, 1039 (2014).

[16] J. Wu and C. Shu, J. Comput. Phys. **228**, 1963 (2009).

[17] S. K. Kang and Y. A. Hassan, Int. J. Numer. Methods Fluids **66**, 1132 (2011).

[18] Y. Hu, H. Z. Yuan, S. Shu, X. D. Niu, and M. J. Li, Comput. Math. Appl. **68**, 140 (2014).

[19] Y. N. Cai, S. Li, and J. H. Lu, Int. J. Numer. Methods Fluids **87**, 109 (2018).

[20] K. Luo, Z. Wang, J. Fan, and K. Cen, Phys. Rev. E **76**, 066709 (2007).

[21] Z. L. Wang, J. R. Fan, and K. Luo, Int. J. Multiphase Flow **34**, 283 (2008).

[22] Y. G. Cheng, H. Zhang, and C. Liu, Commun. Comput. Phys. **9**, 1375 (2011).

[23] Y. Tang, T. H. Wu, G. W. He, and D. Qi, Int. J. Multiphase Flow **99**, 408 (2018).

[24] G. R. Liu and T. T. Nguyen, in *Smoothed Finite Element Methods* (CRC Press, Boca Raton, FL, 2010), pp. 497–508.

[25] G. G. Le and J. F. Zhang, Phys. Rev. E **79**, 026701 (2009).

[26] J. H. Lu, H. F. Han, B. C. Shi, and Z. L. Guo, Phys. Rev. E **85**, 016711 (2012).

[27] S. Q. Wang, Y. N. Cai, G. Y. Zhang, J. H. Lu, and S. Li, Int. J. Numer. Methods Fluids **88**, 363 (2018).

[28] G. R. Liu and G. Y. Zhang, Int. J. Comput. Methods **5**, 621 (2008).

[29] G. R. Liu and G. Y. Zhang, *Smoothed Point Interpolation Methods: G Space Theory and Weakened Weak Forms* (World Scientific, Singapore, 2013).

[30] Z. L. Guo, C. G. Zheng, and B. C. Shi, Phys. Rev. E **65**, 046308 (2002).

[31] Y. H. Qian, D. d'Humières, and P. Lallemand, Europhys. Lett. **17**, 479 (1992).

[32] X. He and L. S. Luo, J. Stat. Phys. **88**, 927 (1997).

[33] I. Ginzbourg and P. M. Adler, J. Phys. II France **4**, 191 (1994).

[34] G. R. Liu and Y. T. Gu, Int. J. Numer. Methods Eng. **50**, 937 (2015).

[35] J. G. Wang and G. R. Liu, Int. J. Numer. Methods Eng. **54**, 1623 (2002).

[36] T. Belytschko, W. K. Liu, and B. Moran, *Nonlinear Finite Elements for Continua and Structures* (John Wiley & Sons, Hoboken, NJ, 2014).

[37] C. S. Peskin, Acta Numer. **11**, 479 (2002).

[38] Z. L. Guo, C. G. Zheng, and B. C. Shi, Chin. Phys. B. **11**, 366 (2002).

[39] Z. Q. Zhang, G. R. Liu, and B. C. Khoo, Int. J. Numer. Methods Eng. **90**, 1292 (2012).

[40] F. Sotiropoulos and X. Yang, Prog. Aerosp. Sci. **65**, 1 (2014).

[41] S. Turek and J. Hron, in *Fluid-Structure Interaction*, Lecture Notes in Computational Science and Engineering (Springer, Berlin, 2006), pp. 371–385.

[42] K. Nordanger, A. Rasheed, K. M. Okstad, A. M. Kvarving, R. Holdahl, and T. Kvamsdal, Ocean Eng. **124**, 324 (2016).

[43] Z. Q. Zhang, G. R. Liu, and B. C. Khoo, Comput. Mech. **51**, 129 (2013).

[44] J. Sigüenza, S. Mendez, D. Ambard, F. Dubois, F. Jourdan, R. Mozul, and F. Nicoud, J. Comput. Phys. **322**, 723 (2016).

[45] J. Cheng, Philos. Trans. R. Soc., A **353**, 981 (1998).

[46] T. J. Pedley and S. J. Hill, J. Exp. Biol. **202**, 3431 (1999).

[47] S. Kern and P. Koumoutsakos, J. Exp. Biol. **209**, 4841 (2006).

[48] C. J. Wu and L. Wang, Sci. China, Ser. E: Technol. Sci. **52**, 658 (2009).

[49] C. J. Wu and L. Wang, Acta Mech. Sin. **26**, 45 (2010).

[50] E. D. Tytell, C. Y. Hsu, T. L. Williams, A. H. Cohen, and L. J. Fauci, Proc. Natl. Acad. Sci. USA **107**, 19832 (2010).

[51] M. Gazzola, P. Chatelain, W. M. V. Rees, and P. Koumoutsakos, J. Comput. Phys. **230**, 7093 (2011).

[52] W. Q. Wang, R. Yin, D. W. Hao, and Y. Yan, Adv. Mech. Eng. **2014**, 489683 (2014).

[53] B. Dorschner, S. S. Chikatamarla, and I. V. Karlin, Phys. Rev. E **95**, 063306 (2017).